UNIVERSIDADE
BEIRA INTERIOR

Development of a Preliminary Framework for the Evaluation of Oxygen-Hydrogen Combustion Characteristics

(versão corrigida após defesa)

João Ricardo de Sousa Pedrosa

Dissertação para obtenção do Grau de Mestre em
Engenharia Aeronáutica
(mestrado integrado)

Orientador: Prof. Doutor André Resende Rodrigues da Silva

abril de 2023

Declaração de Integridade

Eu, João Ricardo de Sousa Pedrosa, que abaixo assino, estudante com o número de inscrição a38376 de/o Engenharia Aeronáutica da Faculdade de Engenharia, declaro ter desenvolvido o presente trabalho e elaborado o presente texto em total consonância com o **Código de Integridades da Universidade da Beira Interior**.

Mais concretamente afirmo não ter incorrido em qualquer das variedades de Fraude Académica, e que aqui declaro conhecer, que em particular atendi à exigida referenciação de frases, extratos, imagens e outras formas de trabalho intelectual, e assumindo assim na íntegra as responsabilidades da autoria.

Universidade da Beira Interior, Covilhã 04/04/2023

Assinado por: **João Ricardo de Sousa Pedrosa**
Num. de Identificação: 15665220
Data: 2023.04.04 15:38:16+01'00'

Acknowledgments

I would like to express my deepest gratitude to my supervisor, Prof. Dr. André Silva, for his guidance, support, and encouragement throughout the entire process of this dissertation. His expertise, patience, and valuable feedback have been invaluable to me. I also would like to thank Leandro Magalhães for his contributions and insights. His proofreading, suggestions and teachings on the concepts related to this work were truly invaluable.

Lastly, I would like to express my gratitude to my family and friends for their constant backing and uplifting attitude throughout this journey. Their love and understanding were an essential source of motivation.

I am deeply indebted to all of the individuals who have helped and supported me throughout this dissertation. Without their contributions, this work would not have been possible. I am truly grateful for their support.

Resumo

O desenvolvimento de um motor foguete envolve maximizar o seu desempenho e minimizar os custos. Os testes experimentais que fazem parte desse desenvolvimento podem ser dispendiosos e complexos de executar. Por isso, tem existido uma procura por complementar estes testes numéricos com o poder computacional dos computadores através de ferramentas numéricas. Desta forma, é possível direcionar as campanhas experimentais para regiões ou fenómenos de interesse, diminuindo os custos destas. Especificamente, para os motores foguete de propelente líquido, a necessidade de maior desempenho, ou seja, maior impulso específico, levou a um aumento da pressão na câmara de combustão desses sistemas de propulsão. Além disso, hidrogénio gasoso e oxigénio líquido é uma das combinações de propelente que oferece maior desempenho (impulso específico), devido ao elevado poder calorífico, que resulta numa temperatura adiabática de chama elevada, e ao baixo peso molecular. Estas são as razões pelas quais esta combinação de propelente tem sido usada em muitos sistemas de propulsão que utilizam motores foguete de propelente líquido. Neste trabalho, uma ferramenta numérica é desenvolvida para calcular a temperatura adiabática da chama e a composição de equilíbrio químico correspondente, para um determinado valor de pressão e razão de equivalência, para a reação de combustão entre hidrogénio e oxigénio. Como os valores de temperatura são muito elevados, a dissociação dos produtos da combustão é tida em conta. Três equações de reações químicas são consideradas, cada uma com um número diferente de espécies. A composição de equilíbrio químico é calculada através da minimização da energia livre de Gibbs. Uma biblioteca termodinâmica é usada para calcular propriedades termodinâmicas para espécies individuais. Os resultados dos cálculos mostram que um aumento na pressão traduz-se num aumento da temperatura adiabática de chama. Além disso, à medida que o número de espécies aumenta, a temperatura adiabática da chama diminui. A temperatura adiabática de chama máxima é obtida para misturas ligeiramente ricas.

Palavras-chave

Combustão em condições supercríticas, Motor foguete de propelente líquido, Temperatura adiabática de chama, Combustão de hidrogénio-oxigénio

Abstract

Rocket engine development always involves maximizing performance and reliability and minimizing costs. The experimental tests that are part of that development can be costly and complex to execute. Therefore, there has been a search to complement these numerical tests with the computational power of computers through numerical tools. In this way, it is possible to direct experimental campaigns to regions or phenomena of interest, reducing their costs. Specifically, for liquid rocket engines, the need for higher performance, that is, higher specific impulse, led to an increase in the chamber pressure of these propulsion systems. Moreover, gaseous-hydrogen and liquid-oxygen is one the propellant combinations that offers high performance (specific impulse) because of its high heating value, which results in high adiabatic flame temperature and low molecular weight. These are the reasons why this propellant combination has been used in many liquid rocket engine propulsion systems. In this work, a numerical tool is developed to compute the adiabatic flame temperature and the corresponding chemical equilibrium composition for a given value of pressure and equivalence ratio for the combustion reaction between hydrogen and oxygen. As temperature values are very high, the dissociation of combustion products is taken into account. Three chemical reaction equations are considered, each with a different number of species. The minimization of the Gibbs free energy is done to calculate the chemical equilibrium composition. A thermodynamic library is used to compute thermodynamic properties for individual species. Results of calculations show that an increase in pressure translates into an increase in the adiabatic flame temperature. Also, as the number of species increases, the adiabatic flame temperature decreases. The maximum adiabatic flame temperature is obtained for slightly rich mixtures.

Keywords

Supercritical combustion, Liquid rocket engine, Adiabatic flame temperature, Hydrogen-Oxygen combustion

Contents

List of Figures

List of Tables

Nomenclature

A	Area	m^2
c_p	Isobaric Specific Heat	$\mathrm{J\,mol^{-1}\,K^{-1}}$
Da	Damköhler number	-
F	Thrust	N
g_0	Gravitational Acceleration at sea level	$\mathrm{m\,s^{-2}}$
G	Gibbs Free Energy	J
g	Chemical Potential	$\mathrm{J\,mol^{-1}}$
h	Specific Enthalpy	$\mathrm{J\,mol^{-1}}$
h_f^0	Enthalpy of formation	$\mathrm{J\,mol^{-1}}$
Δh_s	Sensible Enthalpy	$\mathrm{J\,mol^{-1}}$
Δh_R	Specific Enthalpy of Reaction	$\mathrm{J\,mol^{-1}}$
ΔH_R	Enthalpy of Reaction	J
I_{sp}	Specific Impulse	s
J	Momentum Flux Ratio	-
$\dot{m}$	Mass flow	$\mathrm{kg\,s^{-1}}$
MR	Mass Ratio	-
$\overline{M}$	Molecular Weight	$\mathrm{kg\,mol^{-1}}$
n	Mol number	mol
p	Pressure	Pa
P_r	Reduced Pressure	-
R	Specific Gas Constant	$\mathrm{J\,kg^{-1}\,K^{-1}}$
$\overline{R}$	Universal Gas Constant	$\mathrm{J\,mol^{-1}\,K^{-1}}$
Re	Reynolds number	-
R_v	Relative Injection Velocity Ratio of Propellants	-
T	Temperature	K
T_r	Reduced Temperature	-
s	Specific Entropy	$\mathrm{J\,mol^{-1}}$
V	Velocity	$\mathrm{m\,s^{-1}}$
We	Weber number	-
γ	Adiabatic Index	-
μ	Dynamic Viscosity	$\mathrm{kg\,m^{-1}\,s^{-1}}$
ρ	Density	$\mathrm{kg\,m^{-3}}$
ϕ	Equivalence Ratio	-

Subscripts

0	Stagnation Condition
e	Nozzle exit
cc	Combustion Chamber
c	Critical
inj	Injection Conditions
t	Nozzle Throat
∞	Farfield

Superscripts

o	Standard-state pressure ($p^o = 1\,atm$)

List de Acronyms

CEA	Chemical Equilibrium with Applications
CFD	Computational Fluid Dynamics
CPU	Central Processing Unit
DLR	Deutsches Zentrum für Luft- und Raumfahrt
FORTRAN	Formula Translation
HHV	Higher Heating Value
LHV	Lower Heating Value
LRE	Liquid Rocket Engine
MATLAB	Matrix Laboratory
NASA	National Aeronautics and Space Administration
NIST	National Institute of Standards and Technology
PAC	Properties and Coefficients
RAM	Random-access Memory
SRE	Solid Rocket Engine

Chapter 1

Introduction

The rocket propulsion system is one of the greatest inventions in human history, which can be attributed to the immense complexity and difficulty of building a rocket engine. It's a remarkable achievement that speaks to the ingenuity and determination of human beings. What may not be immediately recognized is how this type of propulsion affected and improved our daily life. Rocket engines enable propulsion in environments where traditional atmospheric propulsion systems cannot, such as in space [1]. The unlocking of space exploration led to the emergence of a new technology, specifically satellites. As rocket engines helped put satellites into orbit, we can enjoy things in our daily life such as telecommunications, global internet and television coverage, and accurate weather forecasts. However, it does not come down only to day-to-day life luxuries for humans. Also, scientific experiments and research are conducted on the International Space Station and during spacecraft missions, as well as in deeper space exploration, all to gain understanding and expand our knowledge. Many of these missions relied on rocket propulsion systems specifically, the ones that use chemical energy from liquid propellants, such as liquid oxygen (LOx) and gaseous hydrogen (GH2). Moreover, for future space missions, for example, on the Earth's Moon and Mars or deeper space exploration, there will be a need for advanced propulsion systems that provide the demanding performance requirements of those missions, and that is where the development of liquid rocket engines (LRE) comes into the picture [2].

1.1 Motivation

Although LREs have been used successfully for space missions and are subject to continuous development, there is a need for improved performance, efficiency, reusability, and reduced costs for these systems. Furthermore, most of the knowledge on which LREs are built has been acquired from expensive testing [3]. Thus, in response to those needs, there has been a growing effort over recent years to use the computational power of computers and develop numerical tools. These tools are supposed to help the design of rocket engines so that an overall more optimized design is achieved that can be simulated and iterated. This way, many expensive experimental tests can be substituted by just some work on a computer.

However, as it will be explained further, to match those demanding requirements LREs have been built to operate at elevated combustion chamber pressures. These high pressures are sufficient to exceed the critical point of the propellant substances. Furthermore, the phenomenology in the combustion chamber in those conditions is not clearly understood. The numerical tools can not yet be reliable without a detailed understanding of injection and

combustion phenomena at elevated pressures.

Thus, in recent years, a lot of effort has been put into experimental and numerical research to achieve an understanding of the processes that occur in the combustion chamber of an LRE operating at elevated pressures.

The AEROG research group has been employing numerical simulation methods to study the behavior of jets under transcritical and supercritical conditions. Initial research was done by Barata et al. [4] by evaluating the capabilities of a computational method developed for gaseous flows when applied to supercritical conditions for cryogenic nitrogen jets injected into a nitrogen gaseous environment. Further continuation and development of that previous research were also done [5, 6, 7]. More recently, research has been done to study the behavior of turbulence modeling in supercritical conditions [8, 9] or other issues, such as what boundary condition at the injector walls provides a better numerical representation of experimental data [10, 11]. After that, in continuation of what was concluded from these research, a numerical research in which supercritical nitrogen jet behavior is modeled using an incompressible but variable density approach developed for variable density jets was performed by Magalhães et al. [12], following the methodology of Barata et al. [4]. The work was intended to investigate the suitability of this approach by comparing the results with compressible formulations and experimental data. Also, numerical research considering coaxial injection, which better mimics LRE injection, has been done [13]. The research group has been able to gain a deep understanding of the complex dynamics of these jets. However, the research so far has been limited to cold-flow conditions. As the subject of transcritical and supercritical jets is of high importance for LREs, the research group is interested in transitioning from cold-flow to reacting flow numerical simulations by introducing the modeling of combustion. To achieve this transition, the research group will need to adapt their numerical simulation methods to include the chemistry and thermodynamics of combustion. Thus, this work aims to make one of the first steps to achieve that objective by starting the study of oxygen-hydrogen combustion reaction, as this specific reaction provides a high adiabatic flame temperature and has been used in LREs extensively [14].

This transition from cold-flow to reacting flow is a significant step forward for the AEROG group, and it is expected to lead to valuable insights that can be applied to the design and optimization of LREs. The group's use of numerical simulation methods is a powerful tool that allows them to study and progress in this research area.

1.2 Objectives

The main objective of this work is to undertake a preliminary study of oxygen-hydrogen combustion characteristics using a numerical tool. This will begin with the computation of the adiabatic flame temperature and chemical equilibrium composition for the combustion reaction of hydrogen and oxygen. In the end, it is expected to develop a numerical tool that

calculates the adiabatic flame temperature and the chemical equilibrium composition for given pressure and equivalence ratio.

1.3 Overview

The work is divided into a series of five chapters. The first chapter presents the motivation and objectives that led to the completion of this work. In the second chapter, a theoretical review is presented in which fundamental concepts and some scientific research related to supercritical combustion for LREs are shown. The third chapter describes the methodology developed to achieve the objectives of this work. In the fourth chapter, the results and discussion are presented. The fifth chapter presents the main conclusions of this dissertation and some thoughts for future work.

Chapter 2

Theoretical Review

2.1 Liquid Propellant Rocket Engines

Rocket propulsion uses the principle of jet propulsion, meaning a propulsive force is produced by the momentum of ejected matter, according to Newton's third law. Contrary to duct jet propulsion systems, a rocket engine does not make use of atmospheric air as part of generating a propulsive force. By this means, rocket propulsion systems have the particularity of allowing flight in rarefied air and space environments, as opposed to air-breathing jet engines such as turbojets, turbofans, and ramjets. Moreover, rocket engines can deliver performance that can not be matched by any other propulsion system class, specifically for thrust-to-weight ratio and specific thrust (thrust force per unit of frontal area) [14]. Also, rocket propulsion is not only used for acceleration along a flight path. It can also be used in spacecraft for attitude control, spin control, momentum wheel and gyro unloading, rendezvous in space, and stage separation [14].

There are different types of rocket engines, including solid, liquid, hybrid, nuclear, and electric. Each has its own set of benefits and drawbacks. Rocket engines can be classified based on the type of energy source they use (such as chemical, nuclear, or solar) or their intended function (such as booster stages, sustainer or upper stages, attitude control, and orbit station keeping) [14]. It can be difficult to choose the most suitable rocket propulsion system for a specific mission or application because there are many factors to assess, such as the engine's performance, cost, reliability, and maintainability. These design specifications must be carefully evaluated to make the best choice.

The most common energy source for rocket propulsion is chemical energy [14]. A propellant is a substance that is used in rocket engines to produce a propulsive force. The most widely used type of rocket propulsion system is the solid propellant rocket engine (SRE), which is primarily used for military or defense purposes. The next most commonly used rocket propulsion system is the LRE. Liquid fuel-based rocket engines are highly versatile and are frequently used for space propulsion [1]. LRE allow for precise control over the flow of fuel and the resulting thrust produced by the engine [15]. This control is achieved through the use of different types of valves that regulate the flow of fuel and oxidizer into the combustion chamber. The major components of an LRE are the propellant feed system, a combustion chamber, an igniter system, and a nozzle [16]. A schematic view of an LRE is presented in Figure 2.1. As can be seen, both fuel and oxidizer are stored separately in special tanks. These tanks are designed to handle the unique properties of cryogenic fuels and oxidizers, which

must be kept at very low temperatures and high pressures. The fuel provides the energy for the chemical reaction that produces thrust and the oxidizer provides the oxidant needed to support combustion of the fuel. This chemical reaction is called a combustion reaction in which a fuel undergoes oxidation by reacting with an oxidizing agent (oxidant), resulting in the release of energy. The propellants are ignited in the combustion chamber, resulting in a mixture of hot, high-pressure combustion products. The velocity of this mixture is relatively low, essentially zero [17], as the fuel and oxidizer need to mix and react with each other, contrasting to the very high speeds at the nozzle. As a result, the temperature and pressure in the combustion chamber are approximately equal to the stagnation temperature (T_0) and pressure (p_0).

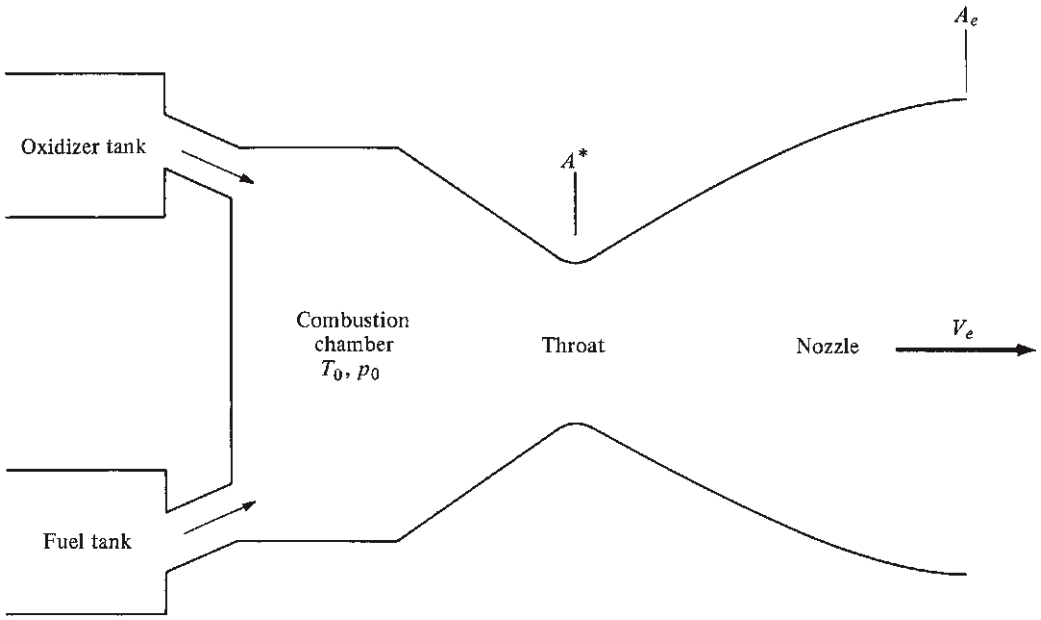

Figure 2.1: Schematic of a liquid rocket engine [17]

The combustion products are then expanded in a convergent-divergent nozzle at supersonic speeds. When the rocket engine ejects a high amount of mass at high speed, the rocket gains an equal amount of momentum in the opposite direction. The propulsive force or thrust (F) is given by [17]:

$$F = \dot{m}V_e + A_e(p_e - p_\infty) \quad \textbf{(2.1)}$$

Two terms define thrust, one is the product of the mass flow rate of combustion products ($\dot{m}$) and the exhaust velocity (V_e), and the other is the pressure difference between the nozzle exit (p_e) and the environment (p_∞) acting over the nozzle exit area (A_e). In vacuum of space ($p_\infty = 0$), pressure thrust will be maximum. However, when flight occurs in the Earth's atmosphere, the exit pressure can be lower than the ambient pressure, which leads to a lower produced thrust. This is an important aspect when designing rocket engines.

Specific impulse (I_{sp}) is an essential parameter that measures and compares the performance or efficiency of different rocket propulsion systems. This parameter evaluates how much

propellant mass flow ($\dot{m}$) is required to reach a given thrust and, thus, is defined as thrust per unit of propellant mass flow at sea level [17]:

$$I_{sp} = \frac{F}{g_0 \dot{m}} \quad (2.2)$$

where g_0 is the gravitational acceleration at sea level.

For a given chamber pressure and propellant mass flow rate with a fixed throat area of nozzle, the maximum thrust can be evaluated by differentiating equation (2.1) and using the momentum equation for one-dimensional steady inviscid flow. The result is that when the pressure of the nozzle exit is equal to the environment pressure ($p_e = p_\infty$), the produced thrust is maximum [14]. Thus, substituting equation (2.1) with $p_e = p_\infty$ into equation (2.2) yields:

$$I_{sp} = \frac{V_e}{g_0} \quad (2.3)$$

In order to maximize specific impulse, the nozzle exit velocity should be maximized (equation (2.3)). The nozzle exit velocity and specific impulse can be given, respectively, by [17]

$$V_e = \left[\frac{2\gamma R T_0}{\gamma - 1} \left(1 - \left(\frac{p_e}{p_0} \right)^{\frac{\gamma-1}{\gamma}} \right) \right]^{\frac{1}{2}} \quad (2.4)$$

and

$$I_{sp} = \frac{1}{g_0} \left[\frac{2\gamma R T_0}{\gamma - 1} \left(1 - \left(\frac{p_e}{p_0} \right)^{\frac{\gamma-1}{\gamma}} \right) \right]^{\frac{1}{2}} \quad (2.5)$$

Considering a perfect gas and complete expansion, the maximum nozzle exit velocity is

$$V_{e,max} = \sqrt{\frac{2\gamma R}{\gamma - 1} T_0} = \sqrt{\frac{2\gamma}{\gamma - 1} \frac{p_0}{\rho_0}} \quad (2.6)$$

Thus, substituting equation (2.6) in (2.3) leads to

$$I_{sp,max} = \frac{1}{g_0} \sqrt{\frac{2\gamma R}{\gamma - 1} T_0} = \frac{1}{g_0} \sqrt{\frac{2\gamma}{\gamma - 1} \frac{p_0}{\rho_0}} \quad (2.7)$$

In order to maximize exhaust gas speed and consequently specific impulse, from equation (2.7) combustion temperature T_0 should be as high as possible, and the molecular weight $\overline{M}$ should be low as possible ($R = \overline{R}/\overline{M}$). These two parameters are influenced by the used combination of fuel and oxidizer. Furthermore, any fuel-oxidizer combination has its adiabatic flame temperature, that is, the maximum combustion temperature theoretically achievable. Thus, there are few adjustable parameters to change the specific impulse for a given propellant besides the oxidizer-to-fuel ratio. Thus, high heating value fuel with the least molecular weight tends to have a high specific impulse. From table 2.1, it can be seen that hydrogen

is the fuel that has the best heating value and lowest molecular weight, making it a very considerable choice. Returning to equation (2.5), there is another important variable that

Table 2.1: Higher (HHV) and lower (LHV) heating values of some LRE fuels at 298.15 K and respective molecular weight [14].

Fuel	HHV [MJ/kg]	LHV [MJ/kg]	Molecular Weight
Hydrogen	141.80	119.96	2
Methane	55.50	50.00	16
Kerosene	46.20	43.00	175

influences specific impulse, that is, the chamber pressure (p_0). This parameter is controlled by the mass flow of propellants being pumped into the chamber from the fuel and oxidizer tanks, and the area of the nozzle throat [17]. It can be seen in equation (2.5) that an increase in the chamber pressure (p_0), increases the specific impulse.

The evaluation of the continuity equation at the throat of a convergent-divergent supersonic nozzle results in the following equation [17]:

$$\dot{m} = \frac{p_0 A_t}{\sqrt{T_0}} \sqrt{\frac{\gamma}{R}\left(\frac{2}{\gamma+1}\right)^{(\gamma+1)/(\gamma-1)}} \quad (2.8)$$

When sonic flow (Mach number equals to one) is present at the throat of a convergent-divergent supersonic nozzle or, in other words, the nozzle is choked, equation (2.8) reveals that the mass flow through that nozzle is directly proportional to p_0 and A_t and inversely proportional to the square root of T_0. Noting that for a fixed nozzle design A_t is constant and that T_0 is fixed by the chemistry, from equation (2.8) it follows that:

$$p_0 = (const)(\dot{m}) \quad (2.9)$$

Thus, from equation (2.9), the chamber pressure is directly proportional to the mass flow of propellants $\dot{m} = \dot{m}_{fuel} + \dot{m}_{oxidizer}$.

LREs have the characteristics of high specific impulse, multiple restart capability, multiple usage, and adjustable thrust. For those reasons, liquid propellants have been frequently used in rocket propulsion systems. Figure 2.2 illustrates that propellant combination and mixture ratio are very influential when high specific impulse is needed. In this figure, propellant combinations can be grouped according to the specific impulse obtained. The first group would include the LOX-LH2 propellant combination, which provides the highest specific impulse by a considerable margin. The next grouping would be the one that combines hydrocarbons with LOX, noting that the higher the carbon content, the lower the specific impulse. With even lower specific impulse comes the LOX-alcohols propellant combination group followed by the ones that use hydrogen-peroxide (H2O2) as an oxidizer. From Figure 2.2, it is clear that the propellant combination of oxygen and hydrogen is the one that provides the best performance in comparison to other options. However, the usage of hydrogen as a fuel for LREs imposes some challenges. One of the main issues with hydrogen is that at ambient

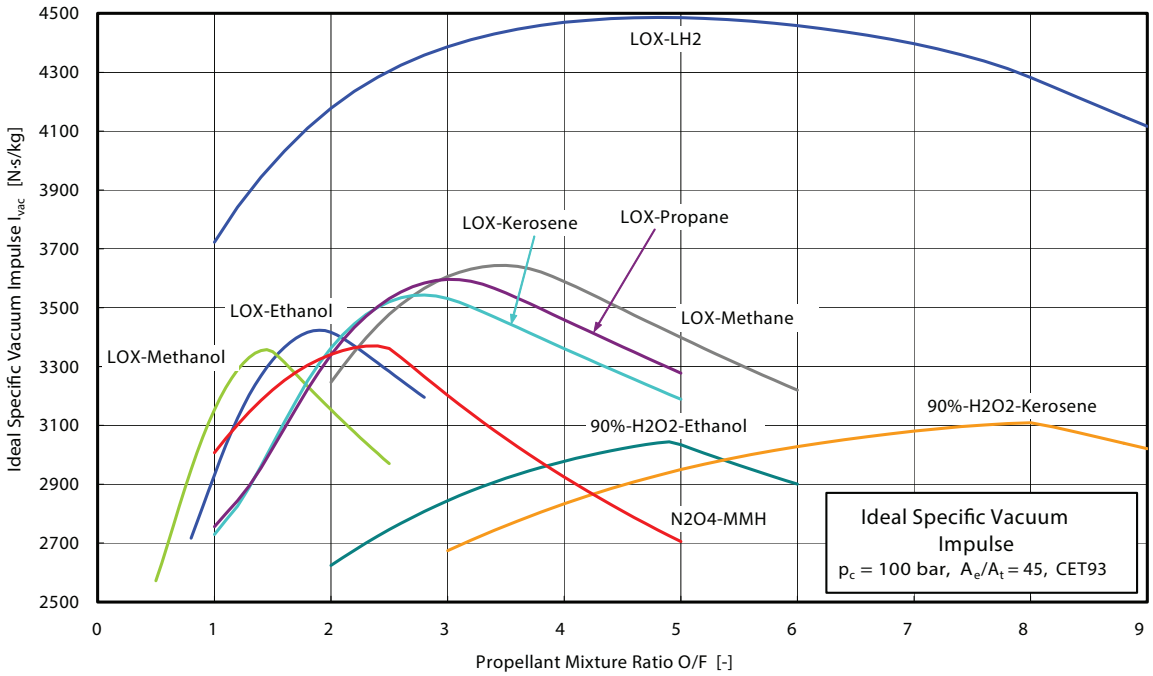

Figure 2.2: Ideal specific impulse of various propellant combinations [18]

temperature it takes a gaseous form. Therefore, carrying hydrogen gas in huge tanks would make the space rocket vehicle bulky, and the only solution is to liquefy the hydrogen. The liquefaction of hydrogen results in a compact tank size.

To achieve this, liquid hydrogen has to undergo a long sequence of processes. Compressors, condensers, and throttling devices work together to bring the temperature down to negative 253 °C. Gaseous hydrogen can only turn into liquid form at this extremely low temperature. This liquid propellant is then transported in huge tanks and stored near the launch station, where it is transferred into the rocket fuel tanks right before the launch.

The liquid hydrogen and liquid oxygen can be directly supplied to the combustion chamber in what is called a pressure fed engine cycle [14]. However, this type of design has limitations such as low thrust, burn times, and throttling capabilities. Also, high pressure tanks would be needed.

To achieve higher pressures, the use of a pump for each substance started to be a feature of LREs. However, some energy is needed to run the pump. A clever way to do that is to run the pump using a turbine that operates on expanded hydrogen. Moreover, for efficient burning, liquid hydrogen has to be converted into gaseous form. In order to get the expanded hydrogen, the liquid hydrogen needs to be circulated around the hot nozzle and combustion chamber. This hot gas is then sent into the combustion chamber. This configuration is called the closed expander cycle engine. The same technique is used to send liquid oxygen to the combustion chamber. In other designs, the gaseous hydrogen is divided. One part goes to the turbine and then exhausted to the atmosphere and the other part goes directly into the

combustion chamber. In this case, it is the open bleed expander engine cycle [19].

With both expander cycles, liquid hydrogen cannot be pumped at a great speed using this method [19]. Another way to run the turbine is to burn a part of the fuel and use its exhaust to drive the turbine. To achieve this, a pre-burner is added. A small portion of liquid propellants are burned, and its high-speed exhaust gases are used to run the turbine. This engine cycle is known as the gas generator cycle. Instead of using a pre-burner in other designs, the turbine is driven by hot combustion gas, which is tapped off from the combustion chamber. This is called the combustion tap-off cycle.

However, these configurations are not very efficient as some exhaust energy is totally lost [14]. The efficiency can be increased by diverting this exhaust from the turbine to the combustion chamber. Here a very small percentage of oxygen is used to burn the hydrogen. This partial burning of hydrogen increases its temperature and pressure, and then, this fuel-rich mixture is completely burned into the combustion chamber. This arrangement is called the staged combustion cycle. This engine type gives the highest thrust and specific impulse [14]. However, the pressure inside the combustion chamber is very high. Therefore, it needs very powerful and expensive parts. Engine cycles are chosen for a particular rocket according to each mission's requirements. Furthermore, a device called an injector plate is used to

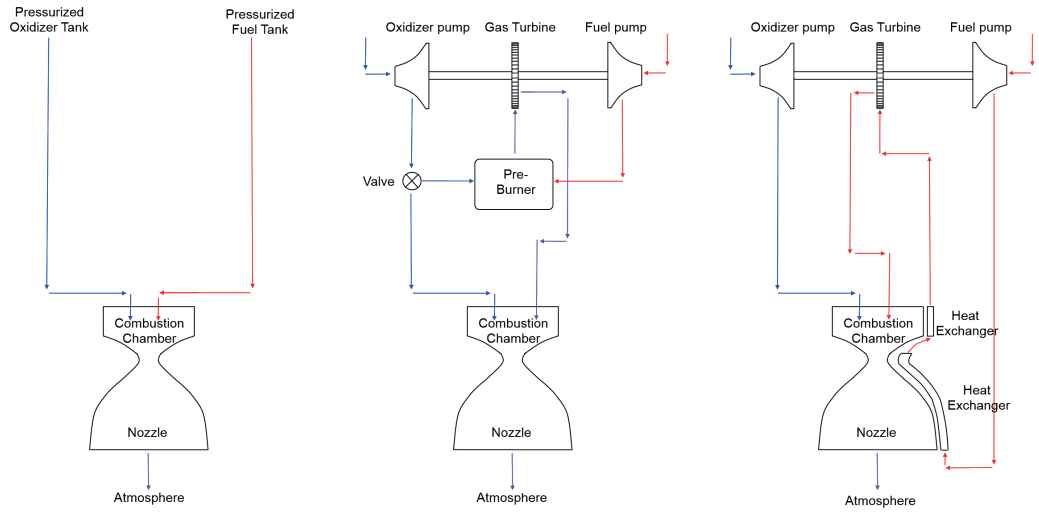

Figure 2.3: Closed rocket engine cycles [19]. Left: pressure fed cycle; Middle: staged combustion cycle; Right: closed expander cycle.

mix hydrogen and oxygen thoroughly in the combustion chamber. Here the propellants get atomized. After the atomization, the propellant is burned. The temperature inside the combustion chamber can reach as high as 3000 °C, which can cause material damage. However, the circulating liquid hydrogen around the combustion chamber helps to maintain the material temperature within the allowable limit.

For a cryogenic rocket engine, the oxygen to hydrogen mass ratio is of the utmost importance. The turbo pump does this crucial job and is therefore known as the heart of a cryogenic en-

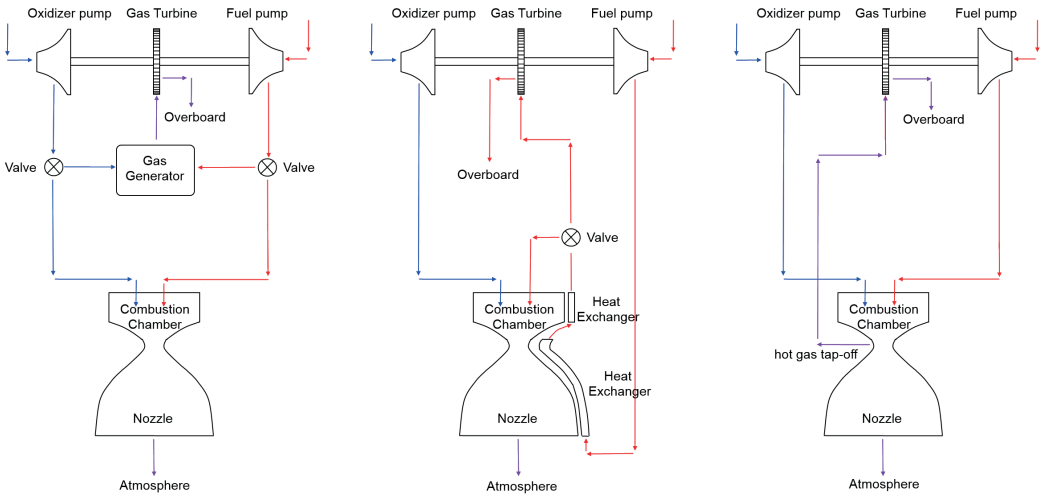

Figure 2.4: Open rocket engine cycles [19]. Left: gas generator cycle; Middle: open bleed expander cycle; Right: combustion tap-off cycle.

gine. The trick with turbo pump design is that the pumps that control the propellant flow rate are controlled by a turbine which is in turn controlled by propellant combustion. A problem within the problem. This tricky pump speed control makes controlling the propellant ratio extremely difficult, which is one big design challenges. Some turbo pumps even use a gearbox to run the pumps at different speeds than the turbine.

Another big design challenge in LRE is thermal insulation [20, 21]. There is a very high temperature gradient in many parts of the rocket engine. For example, the propellant feed system has very low temperatures, as cryogenic fluids are circulating around, and at the combustion chamber and the convergent-divergent nozzle, there are very high temperatures resulting from combustion. In order to prevent heat flux between these components so that they can work at their optimal conditions, strong thermal barriers should be designed. Moreover, is not only essential to take into account this high temperature gradient inside an LRE but also heat flux that may come from outside the rocket, such as the Sun, and aerothermal loads during the ascent through the atmosphere. This kind of high temperature gradient is not common in other rocket engines, making the design of the thermal insulation unique to cryogenic rocket technology.

Rocket engines are designed specifically for the requirements of the launching concept, and changes or improvements to the engine can affect the entire launch system [18]. Additionally, improving the engine's performance may not necessarily lead to an overall improvement in the efficiency of the launcher. Furthermore, in order to achieve higher velocities and payload, space vehicles are often multistaged [14]. This means that the vehicle is divided into two or more stages, each with its rocket engines and propellant so that when a stage runs out of propellant, it is jettisoned. Typically, there are two main ways that each stage can be arranged: series (or tandem) and parallel staging. The former is based on mounting each stage on top of another, and the latter is based on placing a stage alongside another. Commonly,

stages are designated as a booster, first, and upper stage, depending on their purpose of operation. The booster and first stages fire at the launch start to propel the entire space vehicle upwards. The booster stage is usually mounted using the parallel arrangement, consisting of one or more SRE or LRE, and its primary goal is to help the ascent flight at the initial launch phase. When all the propellant of the booster stage is consumed, it is jettisoned, leaving the first stage burning until the end of its propellant and launch phase. Afterward, the first stage is also dropped from the space vehicle, leaving the remaining upper stages that will carry on with its operation. In tables 2.2, 2.3, and 2.4 some booster, first, and upper stage LREs are presented. It can be observed that the LOX/LH2 propellant combination is the one that gives better performance. Moreover, various of these rocket engines operate at chamber pressures that are above the critical point of the propellants, as can be seen specifically from the oxygen and hydrogen critical point values in table 2.5.

Table 2.2: Liquid booster engines [22, 23, 14, 24, 25, 26].

Model	**Propellant combination**	I_{sp} **(sl) [s]**	$p_{chamber}$ **[MPa]**
RD-170	LO2/Kerosene	310	25.1
RD-180	LO2/Kerosene	311	25.5
RD-107	LO2/Kerosene	257	5.9
F-1	LO2/RP1	264	6,6
MA-5A	LO2/RP1	263	4,4
RS-27	LO2/RP1	263	4,8
RD-253	N2O4/UDMH	285	15,2
YF-20	N2O4/UDMH	259	7,4
Viking 6	N2O4/UH25	249	5,9
RS-68	LO2/LH2	360	9,7

Table 2.3: First stage cryogenic rocket engines [22, 23, 14, 24, 25, 26, 27, 28].

Model	**Propellant combination**	I_{sp} **(sl) [s]**	I_{sp} **(vac.) [s]**	$p_{chamber}$ **[MPa]**
RD-108	LO2/Kerosene	252	319	5.1
Viking 5C	N2O4/UH25	249	278	5.9
YF-20B	N2O4/UDMH	259	289	7.4
RS-25	LO2/LH2	-	453	18.9
RS-68	LO2/LH2	-	409	9.7
Vulcain 2	LO2/LH2	-	433	11.7
RD-0120	LO2/LH2	-	454	21.8
LE-7A	LO2/LH2	-	440	12.0
YF-77	LO2/LH2	-	430	10.2

Table 2.4: Upper stage cryogenic rocket engines [22, 23, 14, 24, 25, 26, 29, 30].

Model	**Propellant combination**	I_{sp} **(vac.) [s]**	$p_{chamber}$ **[MPa]**
11D58M	LO2/Kerosene	353	7,6
RD-0210	N2O4/UDMH	327	14.8
AESTUS	N2O4/MMH	325	1,0
J-2	LO2/LH2	421	3.0
RL-10	LO2/LH2	433	2.35
HM7-B	LO2/LH2	444.2	3.5
Vinci	LO2/LH2	465	6.1
YF-75	LO2/LH2	438	3.68
YF-75D	LO2/LH2	442	4.1
LE-5A	LO2/LH2	452	3.98

Table 2.5: Critical temperature and pressure for hydrogen and oxygen [31].

Chemical element	T_{cr} [K]	p_{cr} [MPa]
Hydrogen	33.145	1.2964
Oxygen	154.58	5.043

2.2 Propellant Injection in LREs

2.2.1 The Coaxial Injector

The last component of an LRE, where propellants pass through before reaching the combustion chamber, is the injector. Its purpose is to introduce the propellants into the combustion zone and control their flow to ensure uniform mass flow, atomize liquid jets, and distribute and efficiently mix the propellants to achieve the desired oxidizer-fuel ratio [32].

There are several injector designs like showerhead, impinging element, splashplate, pintle,swirl and coaxial injectors (see Figure 2.5)[15]. The coaxial injector is the most used in LREs, and hence it is the type of injector frequently used for LOX/GH2 injection [33]. The shear coaxial injector is employed by several LREs, for example, the Space Shuttle Main Engine, LE-5, and Vulcain I and II [1]. These engines usually have an injector plate with hundreds of injector elements (Figure 2.6) to provide a large amount of propellant to produce the enormous levels of thrust. A schematic view of the coaxial injector is presented in Figure 2.7. The different diameters are represented by D_0 and D_3, with angle α denoting the degree of taper. The recess length is represented by L_R. If the injector does not have a taper, D_1 will be equal to D_0. The thickness of the LOX post (δ) can be calculated by $(D_2 - D_1)/2$. In a coaxial injector, a central stream of fluid is injected, surrounded by a concentric ring of secondary fluid. For LOX/LH2 propellants, the jet core consists of liquid oxygen, and the surrounding ring comprises gaseous hydrogen. In this type of injector, the liquid oxygen jet core is atomized by the second, high velocity (high Reynolds number), gaseous hydrogen annular jet. The injection in LREs can be characterized by some important dimensionless parameters. The mixture ratio refers to the ratio at which the oxidizer and fuel are mixed and combusted in the chamber to create the hot flow of gases. This ratio impacts the combustion products' composition and temperature, and it is selected to achieve the highest specific impulse. The mixture ratio (MR) is represented as the ratio of the oxidizer's mass flow rate ($\dot{m}_{O_2}$) to the

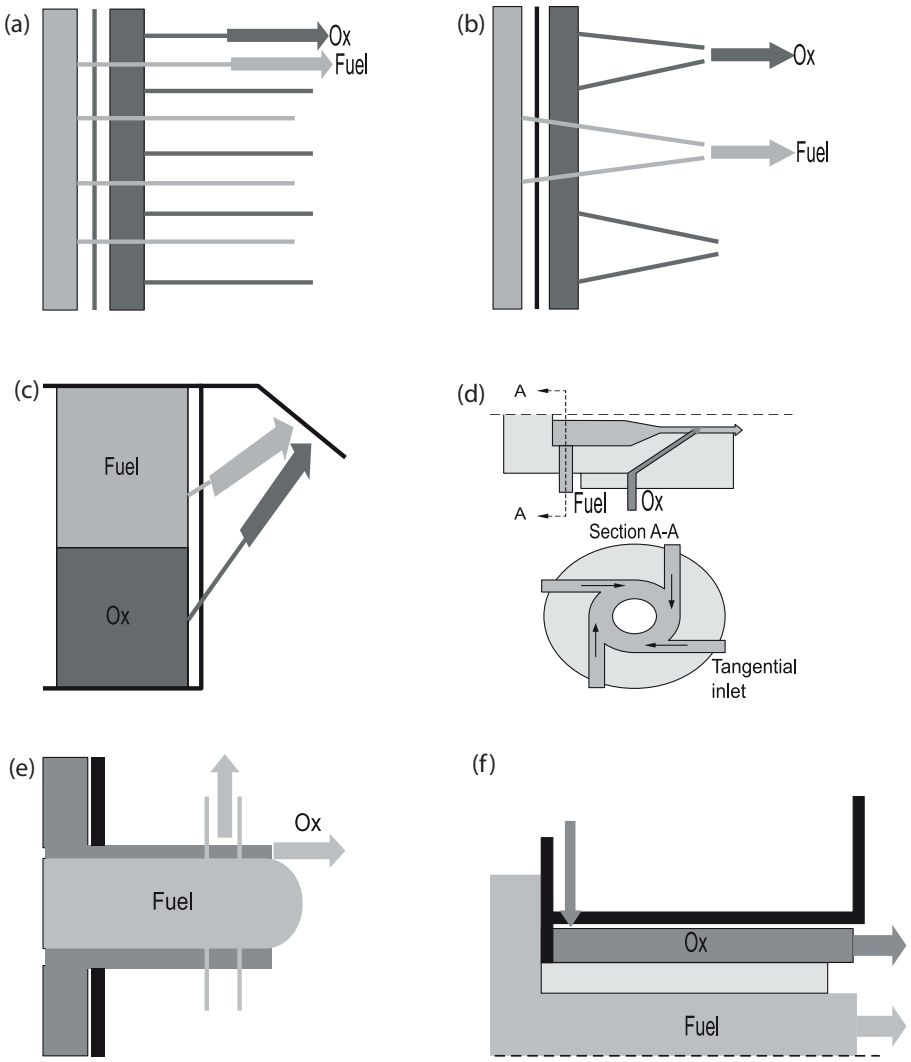

Figure 2.5: Several injector configurations: (a) Showerhead Injector, (b) Like doublet impinging element injector, (c) Splashplate Injector, (d) Swirl bipropellant Injector, (e) Coaxial Injector, (f) Pintle Injector [15].

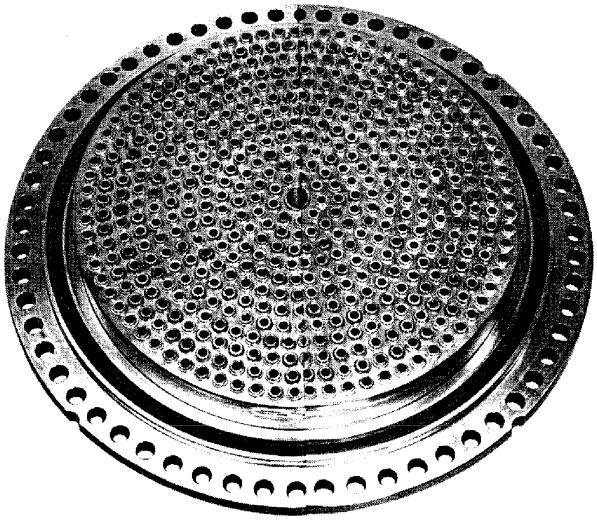

Figure 2.6: Injector plate of the Vulcain LOX/LH2 rocket engine [15].

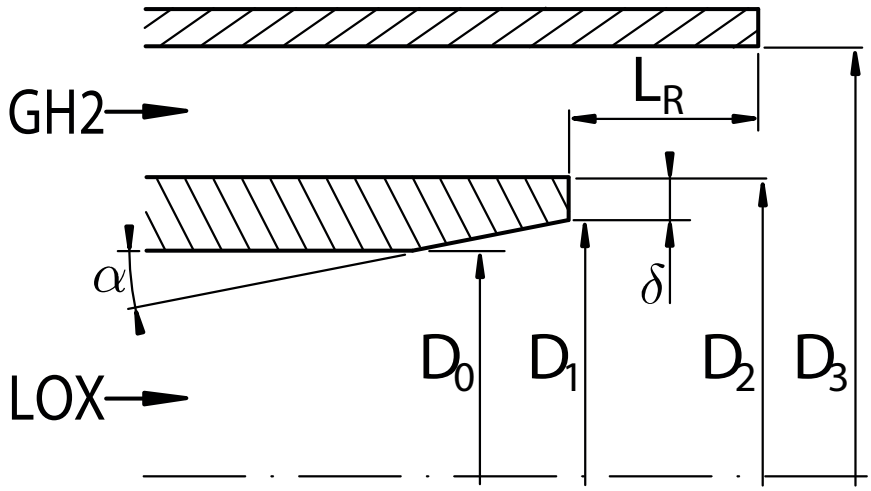

Figure 2.7: Coaxial injector [34].

fuel's mass flow rate ($\dot{m}_{H_2}$):

$$MR = \frac{\dot{m}_{O_2}}{\dot{m}_{H_2}} \quad (2.10)$$

Furthermore, the relative injection velocity ratio (R_v) measures of how the velocity of one propellant being injected into the combustion chamber compares to the velocity of the other propellant being injected. This is an important parameter for characterizing the atomization and mixing efficiency of coaxial sprays and, eventually the combustion stability of LREs [35].

$$R_v = \frac{V_{H_2}}{V_{O_2}} \quad (2.11)$$

Similarly to R_v, the momentum flux ratio (J) compares the momentum of both fluids, the fuel, and the oxidizer. It is used to define operating regimes and characteristics of the combustion process in an LRE that uses coaxial injection [36, 37, 38, 39]:

$$J = \frac{(\rho V^2)_{H_2}}{(\rho V^2)_{O_2}} \quad (2.12)$$

The Reynolds number is the ratio of inertial forces to viscous forces within a fluid subjected to relative internal movement due to different fluid velocities, and it can also be used to characterize shear coaxial injection in LREs. In this case, the Reynolds number of the oxidizer is:

$$Re_D = \frac{\rho_{O_2} V_{O_2} D_1}{\mu_{O_2}} \quad (2.13)$$

A typical LRE has a very high Reynolds number, meaning the flow is turbulent. Additionally, when analyzing combustion in an LRE, it is important to consider the Damköhler number, which can impact propellant mixing, vaporization, and combustion [36]. The Damköhler number is an important parameter in combustion systems because it helps to predict the behavior of the combustion process. The chemical reaction Damköhler number represents

the mixing time relative to the chemical reaction time (equation (2.14)). The vaporization Damköhler number represents the mixing time relative to the vaporization time (equation (2.15)).

$$Da_c = \frac{t_m}{t_c} \quad (2.14)$$

$$Da_v = \frac{t_m}{t_v} \quad (2.15)$$

Usually, shear coaxial injectors have embodied some alterations, such as LOX post tapering and recessing, to enhance performance. These modifications have been investigated experimentally by Mayer and Tamura [40] and Kendrick [41].

2.2.2 Thermodynamic Classification of Injection

Thermodynamic conditions at LREs are such that the thermodynamic critical point of a substance becomes relevant. This point is characterized by the maximum temperature and pressure at which liquid and gas phases can coexist [42]. The critical temperature and pressure for hydrogen and oxygen are presented in Table 2.5. A fluid is supercritical when both pressure and temperature are above their critical values (region (d) in Figure 2.8) [34, 43, 44]. When the temperature is lower than critical temperature and pressure is higher than critical pressure, the fluid is called a transcritical fluid [34, 45, 44, 46], shown as region (e) in Figure 2.8. In addition, region (f) is identified owing to its strong real gas effects caused by the nearness to the critical point [34]. This region is often called transcritical, but to avoid ambiguity with the definition mentioned above of transcritical fluid (region (e) in Figure 2.8), it will be referred as near-critical region. As previously mentioned, hydrogen is preheated before

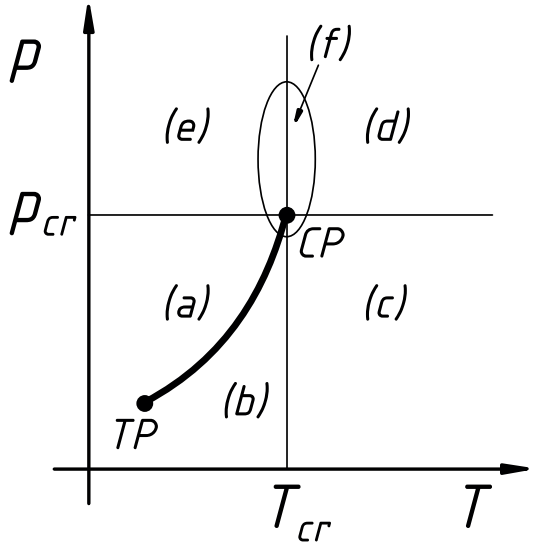

Figure 2.8: Fluid states [34].

injection to a gaseous state. Also, observing chamber pressures from tables 2.2, 2.3, and 2.4 for LREs that use oxygen and hydrogen as propellants, it is seen that it is always higher than

the critical pressure of hydrogen (see table 2.5). Hence, hydrogen is always injected at a supercritical state (region (d) in Figure 2.8). However, the same does not apply to oxygen, as some LREs have chamber pressures above and below oxygen's critical pressure. As oxygen is injected at a temperature below its critical temperature, it can be injected at a subcritical state if the chamber pressure is lower than oxygen's critical pressure or at a transcritical state if the chamber pressure is higher than oxygen's critical pressure (region (a) and (e) in Figure 2.8, respectively). It has been demonstrated that shear-coaxial injection processes in LREs exhibit two distinct modes of combustion, which are determined by the thermodynamic state of injected propellants [45]. More specifically, chamber pressure in relation to the oxygen's critical pressure greatly influences the phenomenology of processes that occur in the combustion chamber so two distinct situations are identified when the chamber pressure is sub- or supercritical in relation to oxygen's critical pressure.

When the operating pressure is low (subcritical), the process of breaking up and atomizing the jet is mainly influenced by aerodynamic (inertial) forces. The momentum exchange between the propellants, caused by the high velocity of the surrounding gaseous hydrogen, helps to atomize the propellants [45]. However, when the pressure exceeds the critical pressure of all propellants, the processes that control combustion in a typical LRE, such as atomization, mixing, vaporization, and ignition, behave differently depending on the relationship between the chamber pressure and the critical pressure of the propellants [40, 46].

2.3 Coaxial Injection at Trans- and Supercritical Conditions

2.3.1 Pure substance behavior

An approach to represent the behavior of a pure substance is through the use of three independent thermodynamic properties such as pressure, temperature, and volume. The phase diagrams for hydrogen and oxygen are presented in Figures 2.9 and 2.10, respectively. It should be noted that the sublimation curve is not included in these diagrams, as for the cases of hydrogen and oxygen, the pressure values on that curve are very small (10^{-3} and below order of magnitude). The phase diagram is a visual representation of the physical states of a substance under varying temperature and pressure conditions. A phase change occurs when a process crosses a curve on the phase diagram. Equilibrium between two phases of the substance is existent on the curves. Each pure substance has its own unique phase diagram.

In these diagrams, there are two significant points: the triple point and the critical point. The triple point, located at the intersection of the solid-vapor, solid-liquid, and vapor-liquid saturation lines, is where all three phases (solid, liquid, and vapor) coexist simultaneously. This point is not important because only liquid and gaseous phases are present in LREs, and their operating conditions are far away from it. However, the same does not apply to the critical point, and in this case, it is of crucial importance in LREs.

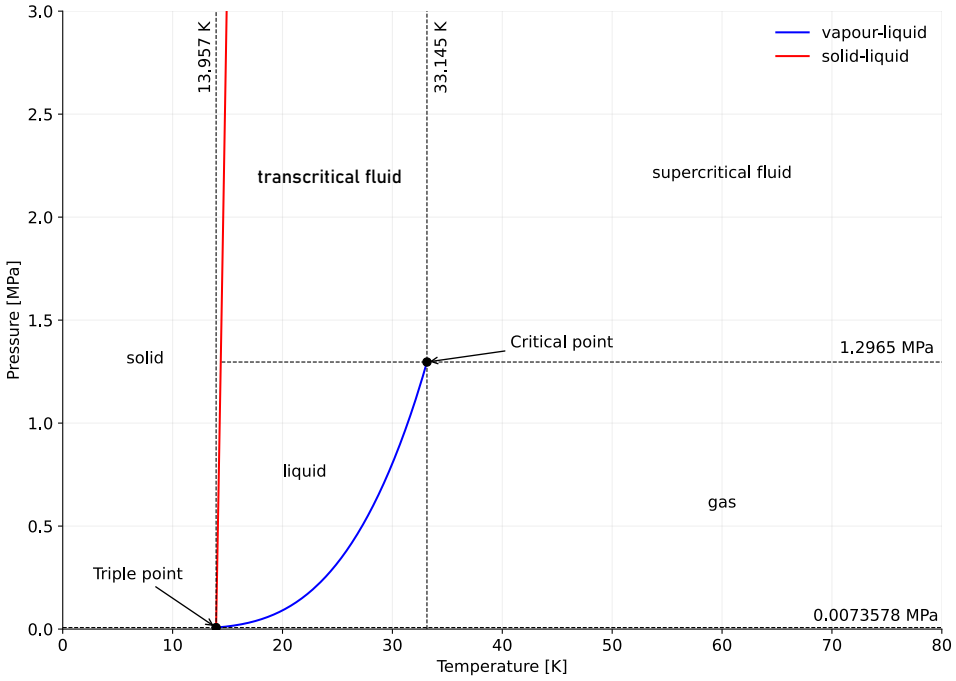

Figure 2.9: Hydrogen phase diagram (data is from [47]).

When the pressure and temperature are close to or exceed the critical values, fluids can exhibit behaviors different from what is typically observed at conditions far from these values

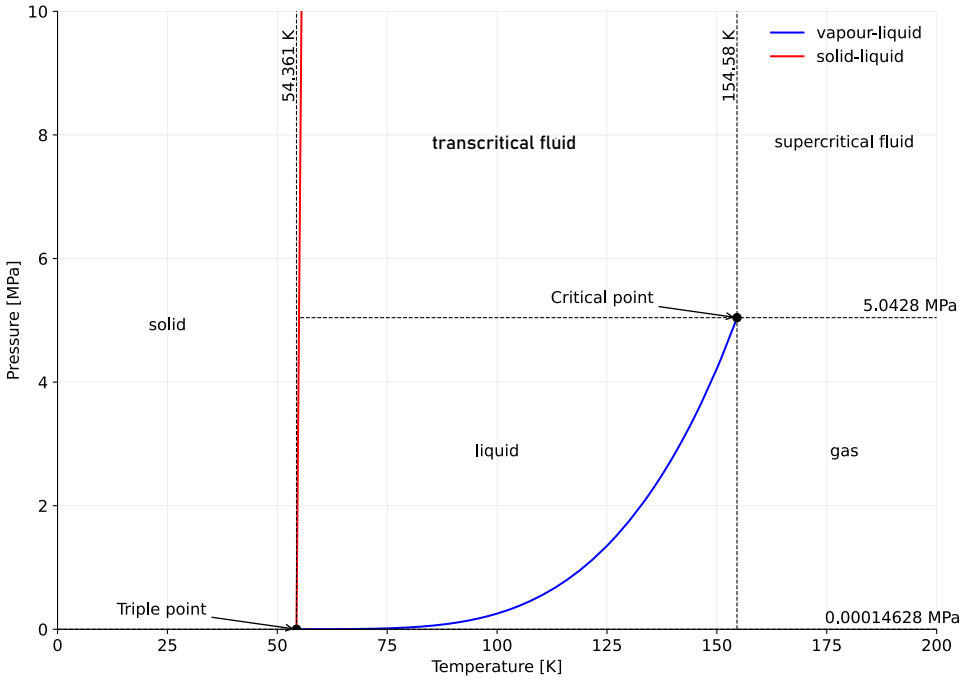

Figure 2.10: Oxygen phase diagram (data is from [47]).

[5]. The critical temperature (T_c) is the point at which it becomes impossible to transition to the liquid phase, no matter how much pressure is applied [8]. The vapor pressure at the critical temperature is called the critical pressure (p_c). The critical point is the end of the vapor-liquid saturation line, where both the temperature and pressure reach their critical values, thus being the highest temperature and pressure at which the liquid and gas phases can coexist in equilibrium. At the critical point, the physical properties of a substance undergo significant changes. The enthalpy required to change a liquid into a gas, known as the latent enthalpy, becomes zero, since both liquid and gas phases no longer exist. In this state, the liquid-vapor boundary that is typically observed at lower pressures disappears. In addition, several other properties, such as mass diffusivity, and surface tension become zero. On the other hand, other properties, such as heat capacity at constant pressure, isentropic compressibility, and thermal conductivity, become infinite [48, 49]. These unusual behaviors of the substance at the critical point make certain thermodynamic concepts, such as phase coexistence, surface tension, and enthalpy of vaporization, that are typically used to describe the behavior of substances at lower pressures no longer applicable [34]. At the critical point, the liquid and gas phases are no longer distinguishable and cease to exist. This means that when the critical point is reached, there is no longer a separation between the two phases. However, recent research has shown that supercritical fluid states can actually be divided into two regions, one with gas-like properties and the other with liquid-like properties, rather than being homogeneously mixed [50]. Graphical representations of density as a function of temperature for different constant pressure values are presented in Figures 2.11 and 2.12 for hydrogen and oxygen, respectively (data is from NIST Chemistry WebBook

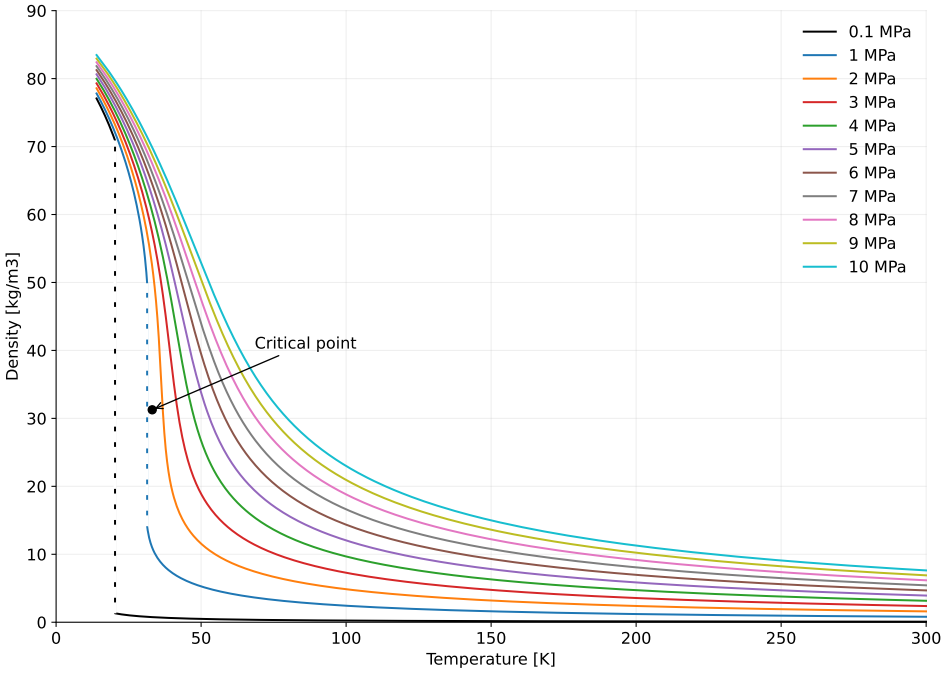

Figure 2.11: Hydrogen density diagram (data is from [47]).

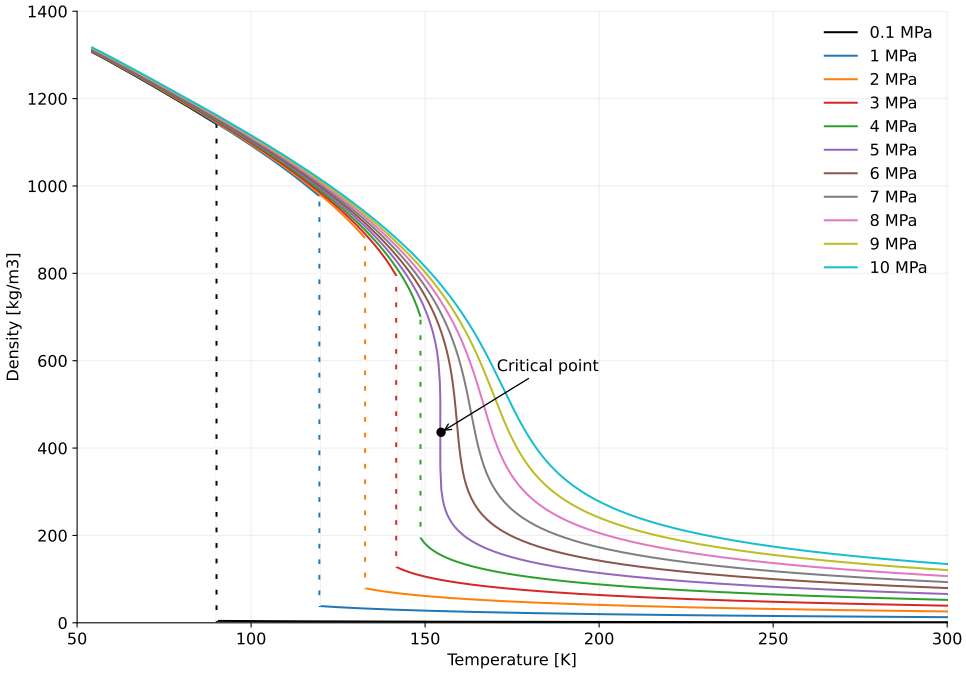

Figure 2.12: Oxygen density diagram (data is from [47]).

[47]). In these graphical representations, the phase equilibrium is represented by the discontinuity on the curves corresponding to pressures lower than the critical pressure. The upper and lower branches represent the liquid and the vapor phase, respectively. When the critical pressure is exceeded, the vanishment of phase equilibrium is seen by the disappearance of the discontinuity. Moreover, the surface tension is also reduced. Temperature changes, especially small increases near the critical point, can have a significant effect on the expansion of the fluid, as shown in Figures 2.11 and 2.12. These temperature changes can also greatly impact the mixing mechanics of the fluid [51]. Research on supercritical fluids has found that when a substance moves through the supercritical region, it changes from liquid-like to gas-like at some point [52]. This suggests that there is an extension of the vapor-liquid saturation line into the supercritical region, called the Widom line [53]. When a substance goes across the Widom line, it is called pseudo-boiling, similar to subcritical boiling (when a fluid's density significantly decreases while it takes a lot of energy to change its temperature) [34]. However, pseudo-boiling differs from subcritical vaporization because it is a continuous process that occurs over a range of temperatures rather than being isothermal. The heat of vaporization vanishes, and the discontinuous phase change is replaced by a continuous, gradual change in properties for isobaric heating at supercritical pressures [54]. Along the Widom line, the density gradient and specific heat capacity have a maximum with respect to temperature. Banuti's work shows an altered phase diagram, where the pseudo-boiling line is a direct continuation of the subcritical vapor-liquid saturation line [34].

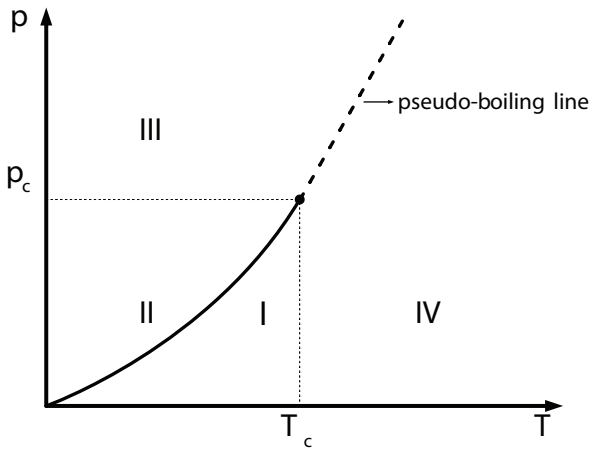

Figure 2.13: Phase diagram with pseudo boiling curve [34].

2.3.2 Cold-flow high pressure injection research

The experimental work from Mayer and Tamura [40] and the numerical work from Oefelein and Yang [55] were one of the first great research made related to LRE supercritical fluid injection and combustion. However, high pressure injection at cold-flow conditions research has been subject to high interest because the absence of the complexities and optical distortions introduced by combustion allows visualization fundamental processes such as atom-

ization, mixing, and jet break-up, even though the realism of combustion is missing [56]. In cold-flow experiments, it is common to use simulants like nitrogen and helium instead of oxygen and hydrogen due to their similar physical properties, non-reactivity and high availability [57]. There has been research done on both small and large-scale conditions to understand and describe the processes involved [58, 59] and to test injector geometries and flow rates similar to those used in actual rocket engines [56, 57]. An outline of high pressure cold-flow injection studies with both single and coaxial jets is provided by Oschwald et al. [44].

When a single substance, such as liquid nitrogen, is injected into a system, the balance between the liquid and vapor phases can be thought of as being influenced by surface tension. This balance, or phase equilibrium, can be affected by the pressure, temperature, and mixture ratio of the fluids present. If the system is made up of a single pure substance, the balance between the liquid and vapor phases occurs when the pressure within the system matches the vapor pressure of the substance and the temperature is equal to the boiling point of the substance [51]. Mayer and Smith [57] found that increasing the pressure of a nitrogen jet led to a decrease in droplets being produced, with no droplets being present once the critical pressure was reached. They also observed the formation of thin, finger-like structures on the surface of the jet that seemed to merge together as the pressure increased. Chehroudi et al. [58] attributed this to a decrease in surface tension and the disappearance of the enthalpy of vaporization at the critical point. Other experiments using LN2 jets at high pressure and a method called Spontaneous Raman spectroscopy to measure the density and estimate the potential core lengths of the core of the injectant were also conducted, such as [60, 61, 62].

Single-element injection studies can give a good understanding of injection at supercritical pressures. However, to understand injection in LREs, the influence of a co-flowing coaxial stream at supercritical conditions needs to be studied, like those created by shear coaxial injectors in LREs. Cold-flow testing is often preferred over combusting environments for these types of studies because it has fewer optical gradients and is cheaper [56, 57].

For a multi-component system at the critical point, the phase equilibrium disappears, and the surface tension decreases. If the temperature increases slightly near the critical point, the fluid expands significantly, resulting in the breakdown of the fluid due to the lack of surface tension and increased heat transfer. Factors such as capillary forces, aerodynamic forces, shear forces, turbulence, and expansion can all contribute to the atomization of the fluid, depending on the injection conditions. Mayer et al. [51] found that at conditions near the critical point, capillary forces are significantly reduced, but droplet detachment can still occur at low injection velocities. At higher injection velocities, shear forces surpass capillary forces, resulting in an injection process comparable to a turbulent gas-like mixing process.

For a multi-component system, a phase equilibrium can exist between a liquid and a gaseous

phase [51], if there is a mechanical

$$p_{gas} = p_{liq} \quad (2.16)$$

a thermal,

$$T_{gas} = T_{liq} \quad (2.17)$$

and a chemical equilibrium of specie i,

$$\mu_{i,gas} = \mu_{i,liq} \quad (2.18)$$

The phase equilibrium diagram for a system of hydrogen and oxygen is shown in Figure 2.14. At a certain reduced pressure, the solubility of hydrogen in oxygen increases with temperature, and the amount of hydrogen in the gas phase decreases. This region is known as the transcritical region [51]. The maximum boundary temperature for the existence of a phase

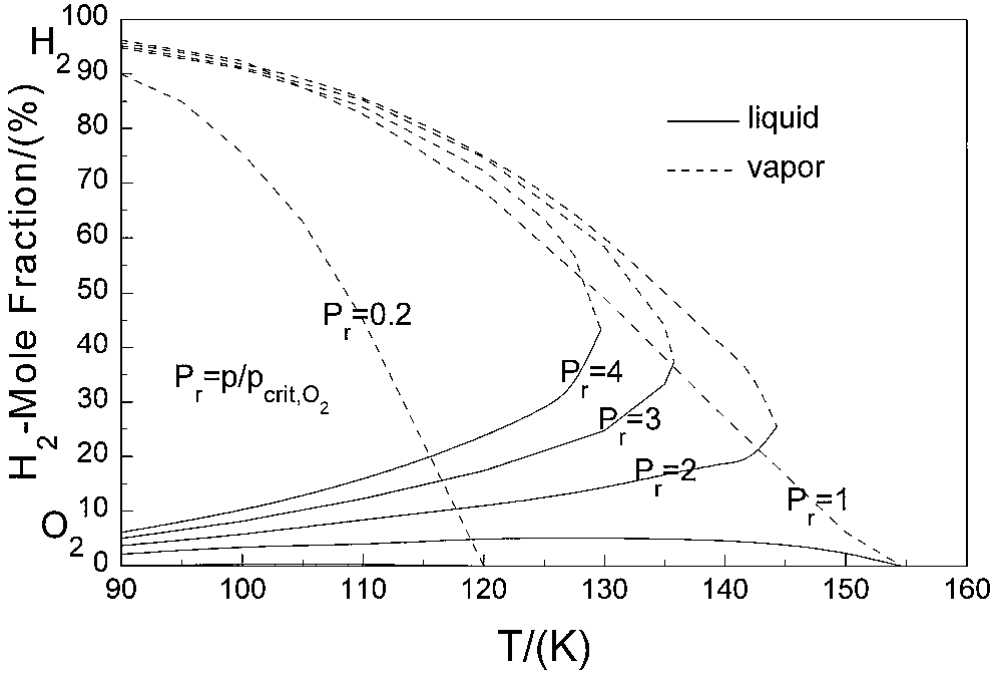

Figure 2.14: Phase equilibrium of O2/H2 system [51].

equilibrium, called the critical mixing temperature, can be found for a binary mixture of oxygen and hydrogen at a given pressure. Above the critical mixing temperature, the fractions of each component in the gas and liquid phases are equal, and supercritical conditions exist. Figure 2.15 shows the critical mixing temperatures at different pressures for various binary systems. In general, the critical mixing temperatures decrease as the pressure increases. The surface tension of the oxygen and hydrogen system is depicted in Figure 2.16, with the saturation line for oxygen shown as a thick line and constant pressure lines for the hydrogen and oxygen system shown as dashed lines. It is important to note that even above the critical pressure, surface tension is present as long as the critical mixing temperature is not exceeded [57]. Studies have shown that at supercritical pressure conditions, the flow is dom-

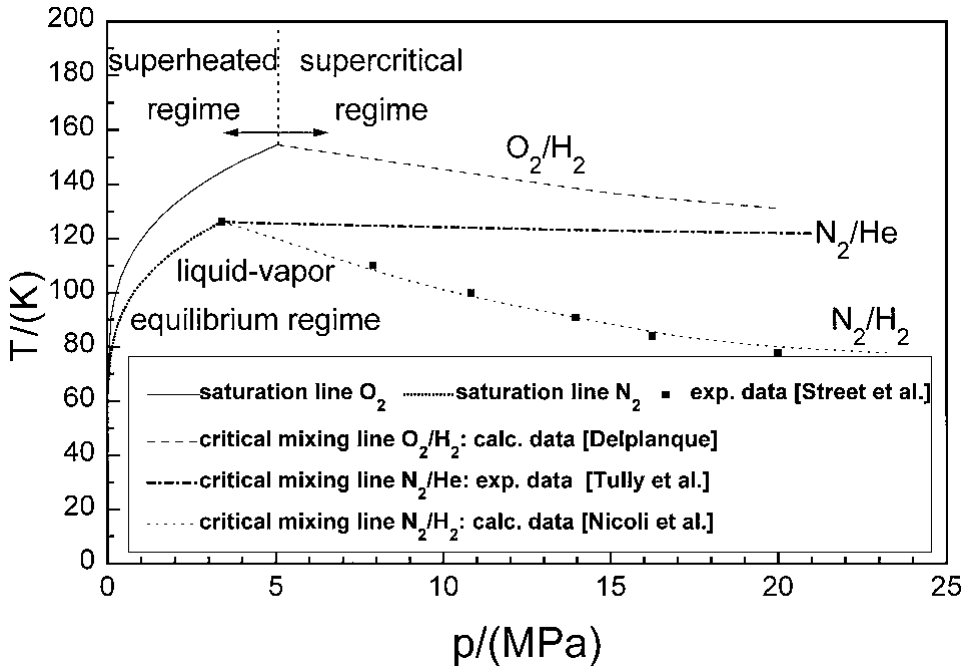

Figure 2.15: Critical mixing lines of different systems [51].

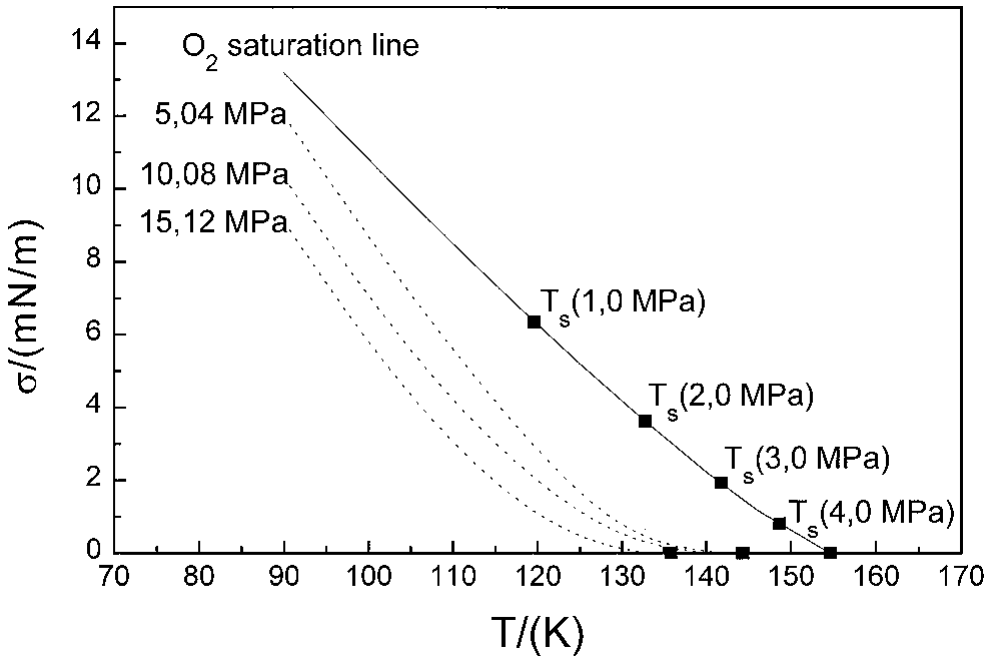

Figure 2.16: Surface tension of the binary O2/H2 system [51].

inated by turbulent gas-like mixing, and no definitive boundary exists between the liquid core and coaxial flow, leading to the formation of sprays at low pressure and dense, light fluid turbulent mixing at supercritical pressure conditions [57].

Heat transfer is important because it can cause changes in density and flow conditions, as demonstrated in the study by Branam and Mayer [63]. The experiment showed that temperature changes had a significant impact on these factors, while pressure and velocity had little effect.

Researchers Oschwald et al. [64], as well as Mayer et al. [62], have conducted studies on the use of coaxial LN2/GH2 in experiments. These studies showed that there were significant temperature differences between the substances being injected, which caused significant heat transfer between the core and surrounding flows. Oschwald and Schik [60] concluded that the temperature of the injection had a greater impact on the development of the jet than the momentum flux ratio.

2.4 Combustion at Trans- and Supercritical Conditions

2.4.1 Experimental test facilities

To better understand and model the complicated combustion processes of cryogenic liquid propellant rocket engines, various testing facilities have been constructed.

2.4.1.1 Mascotte

ONERA developed the Mascotte test facility in the early 1990s [65]. The facility was built in three versions (V01, V02, and V03), each was designed to closely mimic the operating conditions of LREs. The first version of the facility could only operate at low pressures (up to 1.0 MPa) with hydrogen at room temperature. The second version added a heat exchanger to cool the hydrogen down to 100 K. The latest version (V03) can operate at higher pressures up to 7.0 MPa (Figure 2.17). All three versions of the facility have optical access, allowing for measurements to be taken using high-speed photography, shadowgraphy, backlighting, and coherent anti-Stokes Raman scattering under different operating conditions. Extensive testing has been conducted on the first two versions of the facility, providing a large experimental database. The latest version (V03) has allowed for testing at higher pressures, including above the critical pressure of oxygen [67].

In the case of a rocket engine, the Reynolds number of the LOX and GH2 flows can be very large, and the breakup of the liquid jet depends mainly on the momentum flux ratio J. The Weber number (We) plays a key role in determining the size of the droplets produced by primary and secondary atomization. To maintain a consistent momentum flux ratio (J) at different chamber pressures, it is necessary to adjust the mixture ratio of the propellants [65, 67]. The operating points on the Mascotte combustion chamber are presented in Table

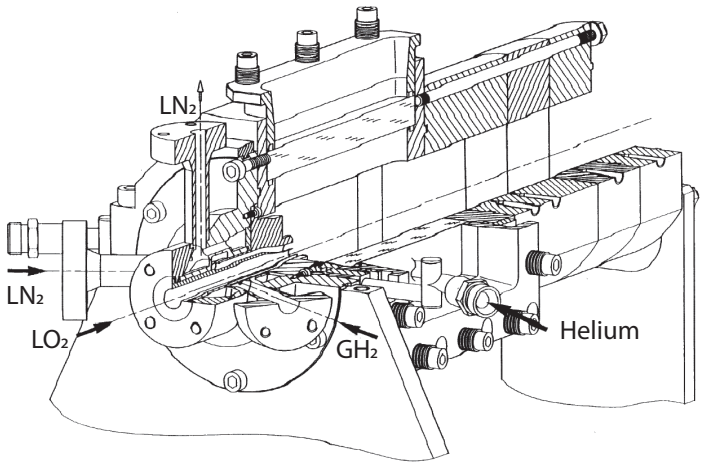

Figure 2.17: Sketch of the Mascotte combustor [66].

2.6. The most important points for studying LOX/GH2 combustion at supercritical conditions are A60 and C60 because their operating is higher than the critical pressure of oxygen and hydrogen. In a recent update, the Mascotte rig was modified (version V04) to allow the

Table 2.6: Mascotte operating points [65].

Point	Pressure [MPa]	flow rate [g/s]	GH2 flow rate [g/s]	J	M
A	0.1	50	15.0	13.4	3.3
C	0.1	50	10.0	6.3	5.0
A10	1.0	50	23.7	14.5	2.1
C10	1.0	50	15.8	6.5	3.2
A30	3.0	50	25	15.5	2.0
C30	2.8	54	17	6.6	3.2
A60	6.7	100	75	16.1	1.3
C60	5.6	100	40	5.5	2.5

injection of methane as well as hydrogen, with a heat exchanger in the fuel feed line that is capable of liquefying methane at a maximum flow rate of 250 g/s [46]. The oxygen flow rate in these experiments can range from 20 to 100 g/s. The combustion chamber is capable of withstanding pressures up to 10 MPa.

2.4.1.2 Pennstate combustor

The GO2/GH2 PennState combustor is a device used for testing at the Cryogenic Combustion Laboratory at Pennsylvania State University [68]. It is designed to simulate the burning of liquid fuels in a full flow staged combustion engine, using two preburners to ignite an oxidizer-rich and a fuel-rich mixture. The hot gases produced by these preburners are then fed into a main combustion chamber [69].

This combustion chamber (Figure 2.18) includes a cylindrical chamber equipped with sensors to measure wall heat flux and a convergent-divergent nozzle [70]. It was created to improve Computational Fluid Dynamics (CFD) tools used in simulations of rocket combustion chambers. They conducted experiments to measure the heat and temperature on the

walls of a rocket combustion chamber using gaseous oxygen and hydrogen as propellants at a chamber pressure and a mixture ratio typical for rocket combustion chambers.

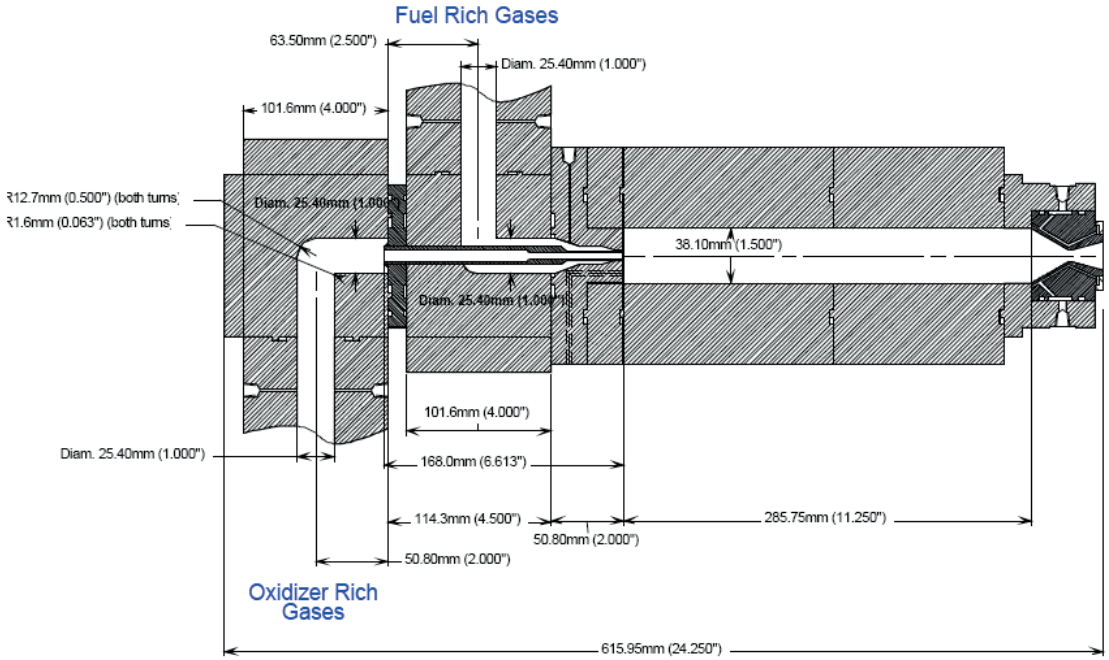

Figure 2.18: Sketch of the Pennstate combustor [71].

2.4.1.3 DLR BKC and BKN combustor

The European test bench P8 is a high-pressure test facility that is used to investigate research and technology related to combustion chamber conditions in modern cryogenic rocket engines. The facility is equipped with systems for supplying propellants, including liquid oxygen, liquid hydrogen, and gaseous hydrogen, at pressures up to 360 bar at the test bench interface. It is capable of controlling the mass flow rates of these propellants at a range of 200 g/s to 8 kg/s for LOX, 50 g/s to 1.5 kg/s for GH2, and 200 g/s to 3 kg/s for LH2 [44]. The BKC single injector combustion chamber was built and tested at DLR Lampoldshausen.

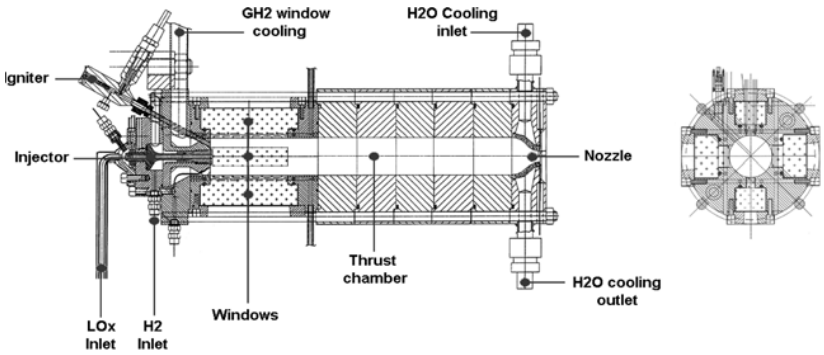

Figure 2.19: Sketch of the BKC combustor [45].

It was created to mimic the operating conditions of real upper stage engines [72]. It has a cylindrical shape and is equipped with a convergent-divergent nozzle (shown in 2.19).

The chamber can be used with different fuel-oxidizer combinations, such as hydrogen and oxygen or methane and oxygen. The pressure within the chamber can be varied from below to above the critical pressure of oxygen. The injection temperature can also be set to range from very cold to room temperature [72]. The BKC model combustor has been used in tests involving the firing of the rocket engine under high pressure, and it features a single coaxial injector head. The combustor is modular in design and includes a module with optical access that allows for the use of non-intrusive diagnostic techniques at pressures as high as 9 MPa. The windows in this module are protected from the high thermal loads of the tests by being cooled with a film of hydrogen at ambient temperature. This cooling method does not affect the flow or combustion processes taking place in the vicinity of the injector [44].

More recently, a new test device was developed, namely the combustor model 'N' (BKN), to address the limitations of past research on rocket combustion chambers with optical access (Figure 2.20). This experiment has been specifically designed for validation purposes and includes various diagnostic tools such as thermocouples and pressure sensors. One unique aspect of this experiment is the large optical window, which is 255 mm long and allows for the first full-length visualization of a flame from a main-stage engine-scaled injector at corresponding mass flows. The inner surface of the window is shaped to match the contour of the combustion chamber wall in order to minimize any disruption to the flow field symmetry within the chamber [73]. To date, only Martin et al. [73] have conducted tests in this combustion chamber at chamber pressures up to 70 bar and ratios of oxidizer to fuel at the main injector up to 6.

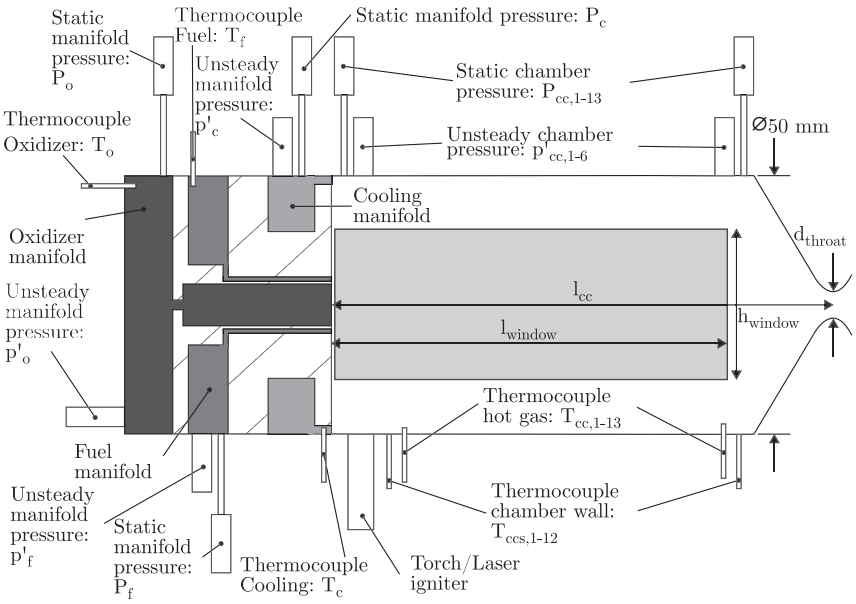

(a) Combustion chamber schematic

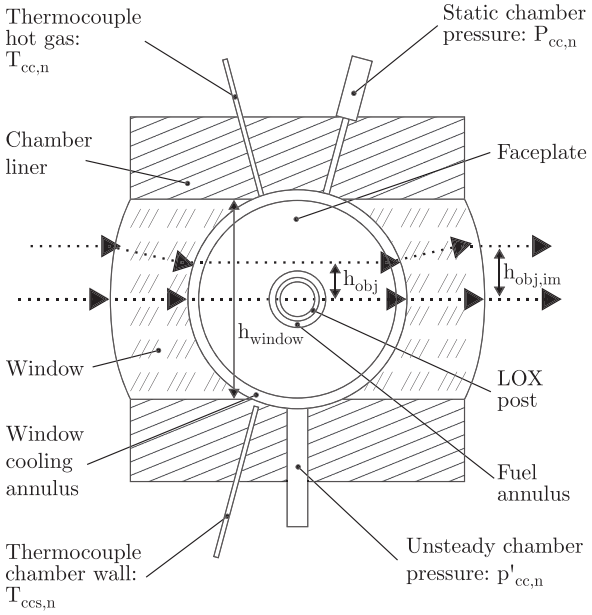

(b) Combustion chamber cross section

Figure 2.20: Sketch of the BKN combustor [73].

2.4.2 Supercritical combustion experimental research

Experimental research on combustion at supercritical pressures has revealed a number of differences compared to subcritical conditions (see Figure 2.21). Table 2.7 presents the operating conditions of several experimental studies. At supercritical pressures, the injection of reactive propellants into a high temperature combusting environment presents various challenges. Mayer and Tamura [40] conducted experiments in which they observed that droplets do not exist at supercritical pressure and that ”snake-like” oscillations and ”thread-like” structures form in the jet flame. They also found that the flame attaches instantly to the LOX post upon ignition and that there is a small but intense recirculation zone behind

the LOX post, which acts as a flame holder. In addition, the effects of injector design on the flowfield were investigated, with the authors concluding that a recessed injector does not significantly improve performance but does create a small, undisturbed combustion chamber that helps to keep the propellants ignited and well mixed. The experiments by Candel et al.

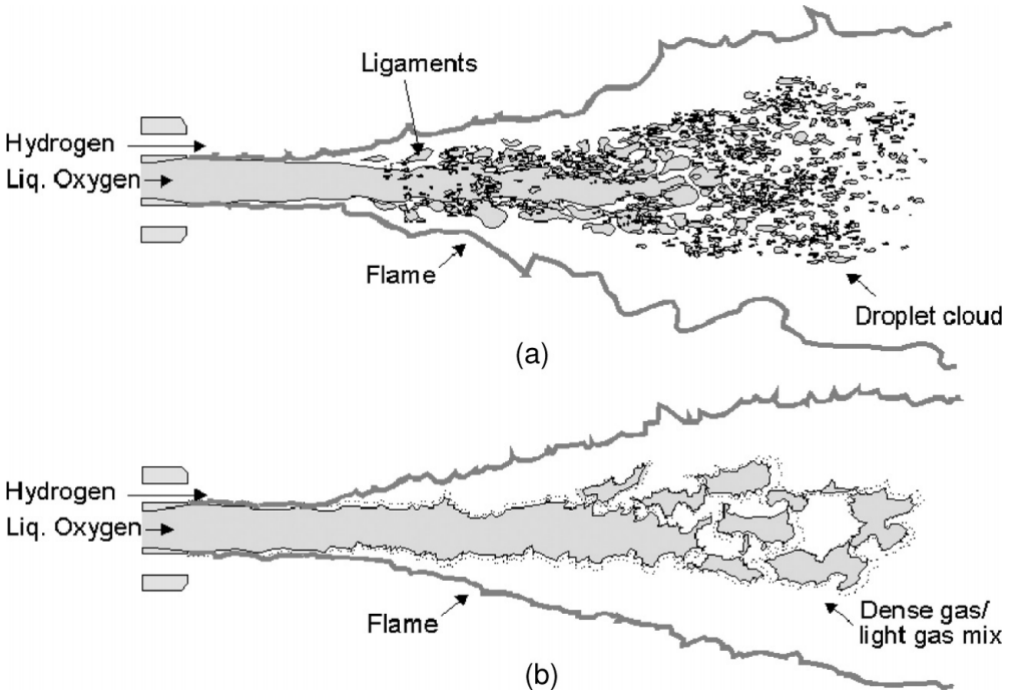

Figure 2.21: Cryogenic jet flames: Subcritical (a) and supercritical (b) [46].

[36] found that at subcritical pressures, flames stabilize in the vicinity of the LOX tube and that the combustion rate is higher than the turbulent mixing rate. Kendrick's [41] experiments showed that recessing the LOX tube by one diameter can improve flame stabilization and increase the width of the flame volume. Mayer et al. [74] hot-fire tests found that the interface between the propellants is separated by a layer of hot reacting gas and that there is a diffusion flame anchored by recirculation zones behind the posts. The radiation intensity of the flame increases downstream, and the spectrum ranges from UV to IR, with little dependency on the mixture ratio of oxygen to fuel. The experiments also found that combustion gases have a wide distribution in gas temperature and composition.

Experiments by Juniper et al. [75] and Smith et al. [38] studied combustion at supercritical pressures, with a focus on cryogenic jet flames and optical diagnostics. The results showed that the rate of combustion at high pressure is influenced by the rate of turbulent mixing rather than vaporization and that temperature distribution was affected by chamber film cooling, a fluctuating flame, and oscillating jet core flow. The maximum temperature observed in the experiments was not in the range of theoretical stoichiometric conditions, and phenomena such as ice and water formation were observed under high pressure conditions. These findings suggest that turbulent mixing and cooling effects play important roles in combustion at supercritical pressures. Ivancic and Mayer [76] conducted experiments and simulations to study the reaction of a shear layer in a combustor at a pressure of 6 MPa. The

simulations showed that the Kolmogorov length scale was around 1 micrometer at the injector exit plane, while the integral turbulent length scale was significantly larger at every point. The length scales also increased downstream of the injector face plate.

Marshall et al. [68] performed experiments on a gas/gas shear coaxial injector element at pressures up to 5.1 MPa to obtain boundary conditions for use in verifying and validating computational fluid dynamics code. These experiments were thorough, including an analysis to define uncertainty limits for all measured mass flow rates and heat fluxes. Conley et al. [77] looked at the behavior of a GO2/GH2 single element shear coaxial injector under different pressure conditions that are commonly seen in rocket engines. They measured various things like heat and temperature at different points in the nozzle and used this information to check the accuracy of computer models that predict how rocket engines burn. Candel et al. [46] discovered that when the pressure inside the chamber of the rocket engine is greater than a certain value (5.04 MPa), the oxygen jets change in structure and become more turbulent, progressing from a subcritical to a supercritical state. The angle at which the flame spreads also becomes smaller at higher pressures, and the momentum flux ratio becomes less important. The rate at which the flame spreads is determined by the amount of interfacial area between the dense oxygen stream and the lighter gas surrounding it and by how quickly the gas is moving and stretching. Recess was found to enhance global instability and mixing in coaxial injectors [46]. According to Smith et al. [78], the way a thrust chamber operates differs significantly depending on the pressure at which it is working. At lower pressure, the liquid oxygen in the core of the chamber tends to have an increase in surface perturbations and flow oscillations, and classical atomization and mixing are more likely to occur. At higher pressures, the flow of propellant in the chamber is less affected by pressure disturbances, regardless of the injection conditions. When the pressure is near or above the critical pressure, the combustion process seems to be very sensitive to the ratio of injection velocities, with values of R_v less than 10 and 20 being particularly problematic at near-critical and supercritical pressure, respectively. Additionally, at supercritical pressure, lower hydrogen injection temperatures can decrease combustion efficiency, but this effect is not seen at lower pressure. According to Nunome et al. [79], unstable combustion can be triggered when hydrogen injection temperatures drop below a certain cryogenic temperature. This transition temperature is higher for a straight-bore liquid oxygen post injector than a taper-reamed injector. Locke et al. [80] studied the primary atomization and combustion characteristics of a liquid oxygen/GH2 shear coaxial injector element at different chamber pressures. They found that the intact dense-oxygen core length was shorter than published correlations for cold-flow conditions. Hardi et al. [81] conducted hot-fire tests using liquid oxygen and gaseous hydrogen at 40 and 60 bar in a rectangular combustor to study flame-acoustic interaction. When transverse acoustic velocity fluctuations were applied to the flame, shadowgraph images showed a shortening of the dense liquid oxygen cores of the shear-coaxial jets.

In their study, Roa and Talley [82] looked at the behavior of flames produced by mixing gaseous hydrogen and liquid oxygen through a coaxial jet. They found that large, annular hydrogen structures formed at the injector exit and curled towards the liquid oxygen jet,

causing an increase in OH emission and vaporizing the liquid oxygen. These annular structures could sometimes even cut off the liquid oxygen jet completely. The speed of the resulting combustion waves varied based on the initial velocities of the outer hydrogen flow and the inner liquid oxygen flow. Suslov et al. [83] conducted experiments using a subscale thrust chamber at various pressure levels, including both subcritical and supercritical conditions. They injected liquid oxygen and gaseous hydrogen at around 120 K and 130 K, respectively, through a single coaxial injector element. They found that the length of the liquid oxygen jet was strongly influenced by the inverse momentum flux ratio (J number). The work of Armbuster et al. [84] found that the flame dynamics of supercritical hydrogen-oxygen combustion are strongly influenced by the acoustics of the oxygen injectors at high chamber pressures. Martin et al. [73] conducted experiments using a research combustor with a large optical window to observe the flames produced by an engine-scaled injector at different pressure levels, such as 43.0, 64.3, and 67.7 bar (Figure 2.22). They collected data on the flame's appearance, as well as temperature, pressure, and unsteady pressure, to validate numerical models. They found that higher momentum flux and velocity ratios resulted in wider flames with steeper angles, which suggests increased mixing. They also observed pockets of combustion products detaching from the flame in the recess of the injector but did not see any negative effects on flame anchoring or combustion stability despite using high momentum flux ratios.

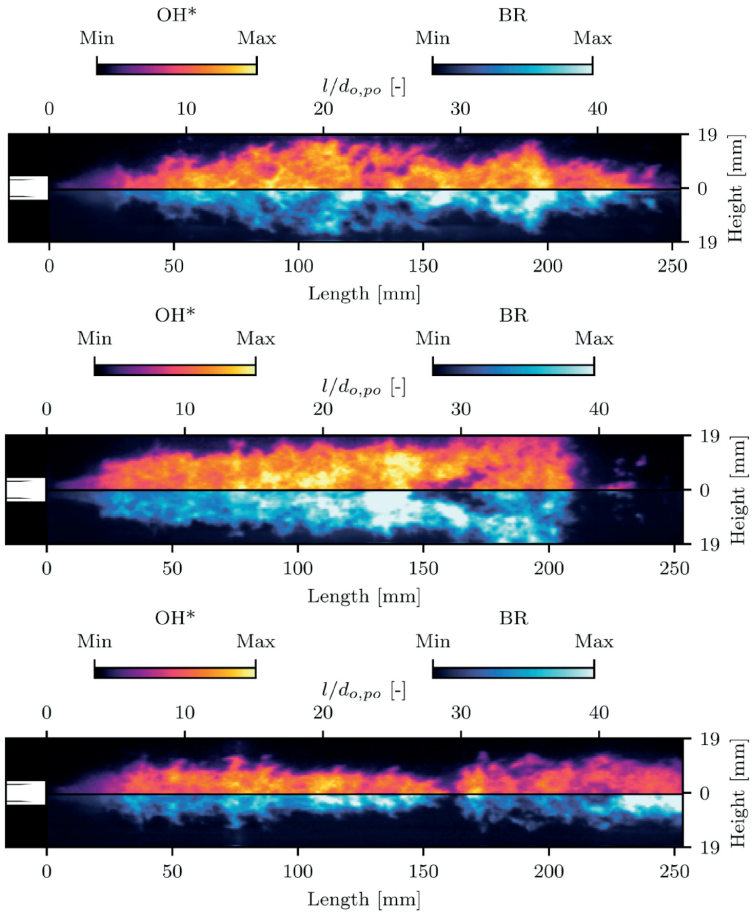

Figure 2.22: Instantaneous flame radiation imaging: 43.0 (top), 64.3 (middle), and 67.7 bar (bottom) [73].

Table 2.7: Operating conditions of coaxial injector hot-fire investigations with oxygen and hydrogen under typical liquid rocket engine conditions.

Researchers	**Pressure [MPa]**	**V_{O_2} [m/s]**	**T_{O_2} [K]**	**V_{H_2} [m/s]**	**T_{H_2} [K]**	**MR**
Mayer et al. [40]	1.0-10.0	10-30	100	200-300	150-300	2-5
Candel et al. [36]	0.1-1.0	1.78-2.23	80	163-893	94-300	2.1-5.3
Kendrick [41]	0.1-1.0	2.23	80	207-308	300	2.1-3.2
Mayer et al. [74]	1.0-10.0	10-30	100	200-300	150-300	2-5
Mayer et al. [51]	6.3	25	127	301	125	-
Juniper et al. [75]	0.5-7	2.2-4.0	80	150-432	280	1.6-4.5
Smith et al. [38]	5.94-6.31	-	95.7-115.5	-	66.7-117	-
Ivancic and Mayer [76]	6.0	25	127	301	125	-
Marshall et al. [68]	2.06-5.17	77.4-142.0	298-700	343.2-795.2	298-811	6.0-6.6
Habiballah et al. [65]	0.1-6.7	-	85	-	300	1.3-5.0
Candel et al. [46]	0.1-6.6	-	85	-	100-298	1.4-5.0
Conley et al. [77]	2.75-6.21	18.97	-	95.67	-	1.33-2.0
Smith et al. [78]	4.0-6.0	-	120	-	130-250	-
Nunome et al. [79]	8.0	-	-	-	-	-
Locket et al. [80]	4.11-6.34	19.14-30.14	111.7-132.8	508.4-523.6	272.2-276.1	6.0
Hardi et al. [85]	4.0-8.0	-	107-140	-	41-300	-
Roa and Talley [82]	3.4	2.4-5.5	138-144	27.5-94	282-288	-
Suslov et al. [83]	4.0-6.21	16-27	114-118	309-444	154-161	4.0-6.0
Armbuster et al. [84]	5.18-8.0	-	113-114	-	103	4.7-4.8
Martin et al. [73]	4.3-6.43	-	114-115	-	161-167	3.4-5.8

2.5 Adiabatic flame temperature computation: Dissociation and Chemical Equilibrium Composition

With the advances in technology and computational power, there has been searching for numerical methods that simulate phenomena like, for example, rocket engine combustion so that a more efficient design process is possible, leading to a higher energy conversion rate and overall a much more efficient rocket engine. In the specific case of the AEROG research group, it is necessary to study the combustion characteristics to introduce the modeling of combustion into their numerical simulations. Then, these can be compared against experimental research, such as the previous section of this work. The computation of the adiabatic flame temperature and chemical equilibrium composition of a combustion reaction is the first step to study its characteristics. In this work, the oxygen-hydrogen combustion reaction is considered.

The thermodynamic equilibrium model is often used to determine the chemical composition of a combustion reaction [86, 87]. It is important to consider that actual combustion reactions do not always proceed to completion at high temperatures. At temperatures above 2200K, some species will dissociate and form new species, which can significantly affect the overall chemical equilibrium. Therefore, it is necessary to take into account a certain number of species when using this model to analyze combustion reactions [88].

Most of the methodology to determine the equilibrium chemical composition necessary for adiabatic flame temperature determination is based on either equilibrium constants like in [89, 90, 91] or minimization of Gibbs free energy like in [92, 93]. According to Jarungthammachote [90], the equilibrium constants methodology involves analyzing a chemical reaction in a system. However, it can be time-consuming and resource-intensive due to the large number of combustion products that need to be considered for a detailed and accurate analysis. On the other hand, the Gibbs free energy minimization methodology involves solving optimization and non-linear equation problems, which requires an understanding of some mathematical theories. The computation of adiabatic flame temperature is usually made by an energy balance and a half-interval search technique [94, 95], as will be seen in the next chapter. Also, the Gibbs free energy minimization technique has been used to obtain other objectives, like in [96]. Other studies related to the chemical kinetics of hydrogen combustion have also been made [97, 98, 99].

Combustion phenomena are an important area of study, and as a result, several programs have been developed to help researchers better understand these processes. Some of these programs are specifically designed to solve chemical equilibrium problems and calculate the adiabatic flame temperature, taking into account the dissociation of gases that occurs during combustion. This information is crucial for understanding the behavior of different fuels under different conditions and can help researchers improve the efficiency and performance of combustion systems. Studying combustion phenomena can also have wider applications,

such as in the development of cleaner and more efficient energy sources or the design of safer and more reliable engines and equipment. In what follows, some computer programs that have been developed are presented.

CEC (Chemical Equilibrium Calculations) is a FORTRAN computer program preceding the very well known CEA (Chemical Equilibrium with Applications) developed by NASA for calculating [100]:

- chemical equilibrium for assigned thermodynamic states (T,P), (H,P), (S,P), (T,V), (U,V), or (S,V);
- theoretical rocket performance for both equilibrium and frozen compositions during expansion;
- incident and reflected shock properties;
- Chapman-Jouguet detonation properties.

CEA (Chemical Equilibrium with Applications) is a widely-used program that calculates the chemical equilibrium compositions and properties of complex mixtures [101, 92, 102], such as reaction systems of oxygen with hydrogen, methane or kerosene. It has a range of applications, including the calculation of theoretical rocket performance, Chapman-Jouguet detonations, and shock-tube parameters for incident and reflected shocks [100]. CEA has been developed over the past 45 years at the NASA Lewis Research Center and is written in FORTRAN, making it compatible with various platforms. It includes a database of transport and thermodynamic properties for over 2000 individual species [103, 104, 105]. An improvement on CEA is that it can simultaneously calculate adiabatic flame temperature and combustion enthalpy along with the equilibrium species, whereas CEC requires these values to be inputted as data. The approach is based on the minimization of free energy and considers condensed phases and gaseous species. A useful program for obtaining thermodynamic input is given in the report [103].

Another example of a program to calculate chemical equilibrium is Gaseq [106]. This a computer program that can solve a variety of problems related to gases, including calculating the temperature and composition of a gas at a given pressure or volume, as well as performing shock calculations and equilibrium constant calculations. However, it is an outdated program that is no longer being maintained, and it does not accurately account for the effects of dissociation on the specific heat of combustion products, which can result in significant errors when predicting the performance of internal combustion engines. To address this issue, the specific heat of combustion products was corrected to take into account the dissociation of these products with temperature, which greatly improved the accuracy of the results.

Additionally, Chemkin is another software package used for simulating chemical kinetics and

thermodynamics [107]. It can be used to model and simulate the behavior of chemical reactions in a variety of environments, including gases, liquids, and surfaces. The software is commonly used in the fields of combustion and propulsion and can be used to model both steady-state and transient systems. Chemkin can also be used to optimize reaction mechanisms, predict reaction rates, and analyze the effects of different operating conditions on chemical reactions. Additionally, Chemkin can be used to calculate the thermodynamic and transport properties of gases.

Furthermore, another example is Cantera which is a suite of object-oriented software tools for problems involving chemical kinetics, thermodynamics, and/or transport processes [108]. It can be used to model combustion, rocket propulsion, gas dynamics, and other processes. The software includes a thermodynamic equilibrium calculator, a kinetic mechanism generator, and a tool for simulating transport properties. Cantera can also be used to simulate multiphase systems and reactions with surface chemistry. It can be used in a variety of programming languages, including Python, C++, and MATLAB.

Chapter 3

Methodology

3.1 Adiabatic Flame Temperature Determination

The adiabatic flame temperature is a measure of the maximum combustion temperature that could be reached in a theoretical combustion reaction, that is, an adiabatic combustion process at constant pressure in which there is no work transfer and no change in kinetic and potential energy [88].

For constant pressure (or constant volume) conditions, the change of chemical reaction energy depends only on the initial and final states of the system, independent of the path taken by the system from the initial state to the final state. Thus, considering a reactive mixture in an open system, with a negligible variation of kinetic and potential energy, and considering that there is only work performed by pressure forces, the first law of thermodynamics allows us to state that, in a process at constant pressure, the energy released or absorbed in a chemical reaction is equal to the enthalpy change of the mixture. Considering that the reactants and products are at the same reference state, that is, the same pressure and temperature, when the reaction occurs, the energy released or absorbed is [88]:

$$\Delta h_R(T) = h_{prod}(T) - h_{reac}(T) \quad (3.1)$$

where Δh_R is the enthalpy of reaction, h_{prod} is enthalpy of products and h_{reac} is the enthalpy of reactants. Considering that the temperature of the reactants is T_1, the adiabatic flame temperature (T_{ad}) can be determined by setting $\Delta h_R = 0$ in equation 3.1:

$$h_{prod}(T_{ad}) = h_{reac}(T_1) \quad (3.2)$$

Noting that enthalpy is equal to the formation enthalpy (h_f^o) at the reference temperature ($T_{ref} = 298.15\,K$) plus the change in sensible enthalpy (Δh_s), that is:

$$h(T) = h_f^o(T_{ref}) + \Delta h_s(T) \quad (3.3)$$

where the sensible enthalpy change is:

$$\Delta h_s(T) = \int_{T_{ref}}^{T} c_p(T^\star)\, dT^\star \quad (3.4)$$

where c_p is the specific heat at constant pressure. Equation 3.2 can be written for each chem-

ical species:

$$\sum_{\substack{j \\ (prod)}} n_j \left(h^o_{f,j}(T_{ref}) + \int_{T_{ref}}^{T_{ad}} c_{p,j}(T)\, dT \right) = \sum_{\substack{i \\ (reac)}} n_i \left(h^o_{f,i}(T_{ref}) + \int_{T_{ref}}^{T_1} c_{p,i}(T)\, dT \right) \quad (3.5a)$$

or, equivalently,

$$\Delta H^o_R(T_{ref}) + \sum_{\substack{j \\ (prod)}} n_j \int_{T_{ref}}^{T_{ad}} c_{p,j}(T)\, dT = \sum_{\substack{i \\ (reac)}} n_i \int_{T_{ref}}^{T_1} c_{p,i}(T)\, dT \quad (3.5b)$$

When the temperature of reactants is not uniform, T_1 is a function of i.

The adiabatic flame temperature determination involves iteratively solving equation 3.5. The methodology is the same adopted in [88]. Two temperatures $T^{(1)}$ and $T^{(2)}$ must be chosen so that $T^{(1)} < T_{ad}$ and $T^{(2)} > T_{ad}$. Expressing equation 3.5 as $f(T_{ad}) = 0$, then $f(T^{(1)})$ and $f(T^{(2)})$ will have opposite signs since enthalpy is a monotonous function of temperature. An estimate of T_{ad}, which will be $T^{(3)}$, can be obtained by the bisection method, that is, $T^{(3)} = (T^{(1)} + T^{(2)})/2$. If $f(T^{(1)}) \times f(T^{(3)}) < 0$, then T_{ad} will be between $T^{(1)}$ and $T^{(3)}$ and the previous can be repeated with $T^{(4)} = (T^{(1)} + T^{(3)})/2$. Otherwise, T_{ad} will be between $T^{(2)}$ and $T^{(3)}$, and these two will be used to compute $T^{(4)}$. The iterative process ends when the two temperatures that bound T_{ad} are close enough with convergence criteria.

3.2 Gibbs Free Energy Minimization

The temperatures involved are quite high so dissociation of combustion products will occur. This implies that the chemical equilibrium composition for each temperature needs to be known. For each specific pressure and temperature thermodynamic states, the rate of dissociation and formation equalize, meaning the chemical equilibrium is achieved. For a thermodynamic process in which pressure and temperature are constant, the equilibrium condition is that the Gibbs free energy is minimum. Thus, the chemical equilibrium composition will be determined by the minimization of Gibbs free energy.

The Gibbs free energy for an ideal mixture of perfect gases is given by [88]:

$$G(T,p) = \sum_{i=1}^{N} n_i \left[g^o_i(T) + R_0 T \ln \frac{p_i}{p^o} \right] \quad (3.6)$$

The fact that the mol number of each species is to be determined and that the total pressure of the mixture is known, equation 3.6 can be rewritten in a more useful form using the following equation [88]:

$$\frac{p_i}{p} = \frac{n_i}{n} \quad (3.7)$$

Thus, equation 3.6 can be simplified to:

$$\frac{G(T,p)}{RT} = \sum_{i=1}^{N} n_i \left[\frac{g_i^o(T)}{RT} + \ln \frac{p}{p^o} + \ln \frac{n_i}{n} \right] \quad (3.8)$$

where the reference pressure is $p^0 = 1\,\text{bar}$.

Now that the objective function is known, the minimization problem can be formulated as the following:

$$min\, G(T,p) \quad (3.9)$$

subject to

$$\sum_{i=1}^{N} a_{ij} n_i = b_j \quad (3.10)$$

This results in a minimization problem with linear equality constraints in which the objective function is non-linear.

3.3 Minimization methodology

The minimization problem presented in the previous section needs to be solved to find the equilibrium chemical composition of all combustion reaction products in order to be able to calculate the adiabatic flame temperature. Thus, an optimization method capable of minimizing a nonlinear multivariable function under linear equality constraints is needed. There are several optimization techniques that fit those conditions.

3.3.1 Gradient method

Considering a function $f : D \mapsto \Re$, D a subset of $\Re^n$. It is supposed that f is of C^1 class in D, and it is intended to minimize function f at D. The gradient of a function f with n variables is [109]:

$$\nabla f(x) = \left[\frac{\partial f(x)}{\partial x_1} \; \frac{\partial f(x)}{\partial x_1} \; ... \; \frac{\partial f(x)}{\partial x_n} \right]^T \quad (3.11)$$

The gradient of a multivariable function at a point x is the direction of maximum rise when moving along the curve of this function from x [110]. A displacement on this curve from x and in the direction of $\nabla f(x)$ results in a greater climb than in any other direction with a path of the same length. For the same reason, a course in the opposite direction of the gradient gives rise to a maximum descent. Thus, it is clear that following the opposite direction to the gradient in the path over the curve of the function, sooner or later, one ends up finding a minimum of this function. The minimization of differentiable functions is generally based on iterative search methods that start from a starting point x_0 belonging to D (usually chosen

arbitrarily) and that define the vector x_{k+1} from of x_k by the formula [109]:

$$x_{k+1} = x_k + \lambda_k d_k \quad (3.12)$$

where $0 < \lambda_k \leq 1$ is the step and d_k is a vector that indicates a descending direction to reach a minimum of the function f. This means that $d_k^T \nabla f(x_k) < 0$ guarantees descent. Note that the basic case is when considering $d_k = -\nabla f(x_k)$. In this case, the algorithm defined by the above equation is called the gradient method since the descent direction is merely the opposite direction of the gradient [110]. At each step of the method, the algorithm moves closer to the minimum value by following the direction indicated by the negative gradient, $-\nabla f(x_k)$, of the function at the current point. The negative gradient indicates in the direction that the function decreases the most quickly. This is based on the assumption that the function $f(x)$ is defined and differentiable in the area around the point x_k. From this, it follows that if $x_{k+1} = x_k - \lambda \nabla f(x_k)$, then $f(x_k) > f(x_{k+1})$, if λ is small enough. Starting with a guess x_0 for a local minimum of f, and considering a sequence x_0, x_1, x_2,... such that $x_{k+1} = x_k - \lambda \nabla f(x_k)$, $k \geq 0$, one gets $f(x_0) \geq f(x_1) \geq f(x_2) \geq$... . This sequence of x_k converges to a desired local minimum if the correct λ value is assigned. The value of λ may change from iteration to iteration. If the function f is convex, then the smallest minimum value (local minimum) is also the overall smallest minimum value (global minimum) for the function.

The stopping condition is when $x_{k+1} \cong x_k$ which by the above equation implies that:

$$\|d_k\| < \varepsilon \quad (3.13)$$

where ε is a small value, for example 10^{-6}.

3.3.2 General scheme of optimization algorithms (for differentiable functions)

The general scheme of optimization algorithms for differentiable functions is [110]:

1. Choose start point x_0 and start at $k = 0$;
2. Calculate the gradient $\nabla f(x_k)$;
3. Determine a descent direction d_k such that $d_k^T \nabla f(x_k) < 0$;
4. Determine a search (or descent) step λ_k;
5. Update the search point as follows: $x_{k+1} = x_k + \lambda_k d_k$, and increment $k = k + 1$;
6. Stop the search if $\|d_k\| \leq \varepsilon$, otherwise go back to step 2.

All differentiable function optimization algorithms try, in general, to find in each iteration a

descent direction d_k and/or a search step λ_k with which convergence to the optimizer (minimizer or maximizer, as the case may be) is guaranteed with an acceptable rate of convergence (usually linear, semi-linear, quadratic, or exponential).

Therefore, from here on, any optimization algorithm has a global scheme similar to the algorithm above, but they are concerned with how to determine the best descent direction d_k (compromise between precision and computational cost, not necessarily the greatest descent direction) and look for a descent step such that $0 < \lambda_k \leq 1$. Step 3 and 4 are what differentiate the algorithms, but steps 1, 2, 5 and 6 are essentially the same.

3.4 Lagrangian method of steepest descent

The optimization problem consists of minimizing a function $f(x, y)$ (equation (3.8)) subject to a constraint $g(x, y) = C$ (equation (3.10)). A way to think about minimizing $f(x, y)$ subject to a constraint $g(x, y) = C$ is to find the contour line (or level curve) $f(x, y) = d$ that tangentially touches the constraint function $g(x, y) = C$ (Figure 3.1) [111]. However, this alone does not solve the problem, and the key to solve this problem is that at the point that these two curves touch the gradient vectors of both functions, $\nabla f(x, y)$ and $\nabla g(x, y)$, are parallel. The reason for this is that the gradient vector of a function at any point is always perpendicular to its curve (Figure 3.1), and points to the direction of the steepest ascent or descent. Thus, as the two gradient vectors are parallel, it can be written that

$$\nabla f(x, y) = \pi \nabla g(x, y) \quad (3.14)$$

where the scalar π is called the Lagrange multiplier [111]. Thus, the possible extreme values

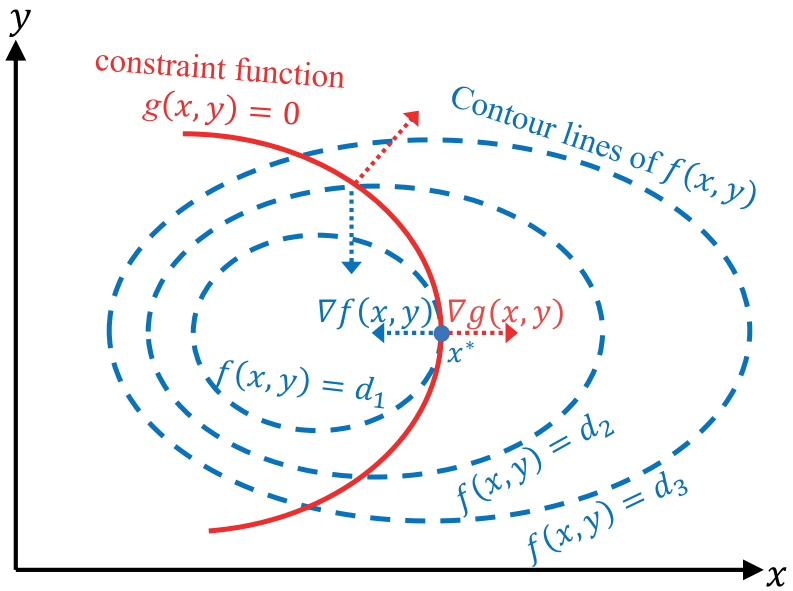

Figure 3.1: Optimization of the function $f(x, y)$ subject to the constraint $g(x, y) = 0$ [111].

of $f(x, y)$ can be found by solving equations (3.14) and $g(x, y) = C$, which in this specific case results in a system of equations with three unknowns (x, y, λ). Then, if more than one

point is found, the function $f(x, y)$ needs to be evaluated at those points to ascertain if they correspond to a maximum or minimum.

It should be noted that minimizing a function $f(x)$ is equivalent to maximizing $-f(x)$ [112].

However, there is a way to encapsulate the problem mentioned above with the Lagrange function [111]:

$$\mathcal{L}(x, y, \lambda) = f(x, y) + \pi(g(x, y) - C) \quad (3.15)$$

In order to evaluate the extreme values of $f(x, y)$, the gradient of the Lagrange function must be zero [112]:

$$\nabla\mathcal{L}(x, y, \lambda) = 0 \quad (3.16)$$

This way can be easier to program into a computer because it turns a constrained optimization problem into an unconstrained one.

The implementation of the Lagrangian method of steepest descent to minimize the Gibbs free energy (equations (3.9) and (3.10)) is similar to other previous works [92, 113, 114]. A set of steps need to be executed iteratively so that at the end of each iteration, there are improved mole number values and a new direction of steepest descent in relation to the last iteration. This set of steps comprises solving a system of linear equations and ensuring that the mole number values are positive.

In order to initialize the iterative solution, a positive set of values for the initial mole numbers, $Y = (y_1, y_2, ..., y_n)$, is required. This can be obtained by solving the mass balance equation (3.17) with as many unknowns as the number of equations, and an initial guess is given to the remaining variables. This will be presented afterward in more detail.

$$\sum_{i=1}^{n} a_{ij} y_i = b_j \; (j = 1, 2, ..., m) \quad (3.17)$$

Following the methodology of [113, 114], two terms from equation (3.8) are enclosed into one variable as follows:

$$c_i = \frac{g_i^o(T)}{RT} + \ln(p) \quad (3.18)$$

where p is the pressure in bar. Also, using c_i, the right side of equation (3.8) is denoted as the variable $f_i(Y)$:

$$f_i(Y) = y_i \left[c_i + \ln\left(\frac{y_i}{\bar{y}}\right) \right] \quad (3.19)$$

where $Y = (y_1, y_2, ..., y_n)$ and

$$\bar{y} = \sum_{i=1}^{n} y_i \quad (3.20)$$

The Gibbs free energy of the mixture (left side of equation (3.8)), $G_{sys}(T)/RT$, is denoted as function $F(X)$, and at the initial set of positive mole numbers Y:

$$F(Y) = \sum_{i=1}^{n} y_i \left[c_i + \ln\left(\frac{y_i}{\bar{y}}\right)\right] \quad (3.21)$$

A Taylor's series expansion about Y is done as $y_i > 0$ [113], resulting in $Q(X)$, which is a quadratic approximation to $F(X)$:

$$Q(X) = F(Y) + \sum_i \frac{\partial F}{\partial x_i}\bigg|_{X=Y} \Delta_i + \frac{1}{2}\sum_i \sum_k \frac{\partial^2 F}{\partial x_i \partial x_k}\bigg|_{X=Y} \Delta_i \Delta_k \quad (3.22)$$

where $\Delta_i = x_i - y_i$, and x_i are the improved mole numbers. Thus, equation (3.22) becomes:

$$Q(X) = F(Y) + \sum_i \Big(c_i + \ln(y_i/\bar{y})\Big)\Delta_i + \frac{1}{2}\sum_i y_i(\Delta_i/y_i - \bar{\Delta}/\bar{y})^2 \quad (3.23)$$

where $\bar{\Delta} = \bar{x} - \bar{y}$. It can be seen that the second partials of both $F(X)$ and $Q(X)$ are positive, and hence both functions are convex [113]. With this, function $Q(X)$ can be minimized subject to the constraints from equation (3.10) using the Lagrange function (equation (3.15))

$$G(X) = Q(X) + \sum_j \pi_j \Big(-\sum_i a_{ij} x_i + b_j \Big) \quad (3.24)$$

Thus, to minimize $G(X)$, following equation (3.16), the first derivatives are equated to zero:

$$\frac{\partial G}{\partial x_i} = c_i + \ln(y_i/\bar{y}) + x_i/y_i - \bar{x}/\bar{y} - \sum_{j=1}^{m} \pi_j a_{ij} = 0 \quad (3.25)$$

The variable x_i is solved from equation (3.25) by combining equations (3.17) and (3.19) with the fact that $\bar{x}$ is the sum of the improved mole numbers. The improved number of moles, x_i, are given as:

$$x_i = -f_i(Y) + \left(\frac{y_i}{\bar{y}}\right)\bar{x}\Big(\sum_{j=1}^{m} \pi_j a_{ij}\Big) y_i \quad (3.26)$$

Summing over i in equation (3.26) results in:

$$\sum_{j=1}^{m} \pi_j \sum_{i=1}^{n} a_{ij} y_i = \sum_{i=1}^{n} y_i \left[\frac{g_i^o(T)}{RT} + \ln(p) + \ln(\frac{y_i}{\bar{y}})\right] \quad (3.27)$$

Using equation (3.19), equation (3.27) can be rewritten as:

$$\sum_{j=1}^{m} \pi_j b_j = \sum f_i(Y) \quad (3.28)$$

If constants are denoted with:

$$r_{jk} = r_{kj} = \sum_{i=1}^{n} (a_{ij} a_{ik}) y_i \quad (3.29)$$

combining equations (3.26), (3.28), and (3.29), the following system of $m + 1$ equations is obtained:

$$\begin{aligned}
&r_{11}\pi_1 + r_{12}\pi_2 + ... + r_{1m}\pi_m + b_1 u = \textstyle\sum_{i=1}^{n} a_{i1} f_i(Y) \\
&r_{21}\pi_1 + r_{22}\pi_2 + ... + r_{2m}\pi_m + b_2 u = \textstyle\sum_{i=1}^{n} a_{i2} f_i(Y) \\
&... \\
&r_{m1}\pi_1 + r_{m2}\pi_2 + ... + r_{mm}\pi_m + b_m u = \textstyle\sum_{i=1}^{n} a_{im} f_i(Y) \\
&b_1\pi_1 + b_2\pi_2 + ... + b_m\pi_m + 0u = \textstyle\sum_{i=1}^{n} f_i(Y)
\end{aligned} \quad (3.30)$$

where:

$$u = -1 + \frac{\bar{x}}{\bar{y}} \quad (3.31)$$

The $m + 1$ unknowns (π_1, π_2, ..., π_m and u) are determined from the system of equations (3.30), and then $\bar{x}$ can be calculated from equation (3.31). With π_j and $\bar{x}$, the improved mole number for each species, x_i, can be computed from equation (3.26). Also, an improved direction of descent is determined by $\Delta_i = x_i - y_i$. Afterwards, x_i is attributed to the variable y_i and the cycle repeats until a predefined error criteria is satisfied. Nevertheless, when the x_i values are calculated from equation (3.26), after solving equations (3.30) and (3.31), there is the possibility of at least one being negative. A procedure that guarantees that all improved mole numbers (x_i) are positive is required. Each iteration cycle starts with the initial positive mole values (y_i) and a new set of improved mole values (x_i) are calculated so that:

$$x_i = y_i + \Delta_i \quad (3.32)$$

A new variable, λ, is introduced to ensure that all improved mole values are positive. This variable takes the highest value between 0 and 1, and defines a fraction of the total distance, $\lambda\Delta_i$, in a way such that all mole number values are positive and nonzero [114]. Thus, when any x_i value is negative, λ performs a correction:

$$x_i^{'} = y_i + \lambda\Delta_i \quad (3.33)$$

In addition to ensuring that all mole numbers are positive, the value of λ is chosen in a way that ensures that the Gibbs free energy of the system decreases, meaning that the minimum point is not passed [114].

Equation (3.19) is rewritten using equation (3.33):

$$f_i(X^{'}) = x_i^{'}\left(\frac{g_i^0(T)}{RT} + \ln(P) + ln\left(\frac{x_i^{'}}{\bar{x}^{'}}\right)\right) \quad (3.34)$$

which can be written in the form:

$$f_i(\lambda) = (y_i + \lambda\Delta_i)\left(\frac{g_i^0(T)}{RT} + \ln(P) + \ln\frac{y_i + \lambda\Delta_i}{\bar{y} + \lambda\bar{\Delta}}\right) \quad (3.35)$$

where $\bar{\Delta} = \bar{y} - \bar{x}$. Summing over i, a new function, $F(\lambda)$, is obtained:

$$F(\lambda) = \sum_i (y_i + \lambda\Delta_i)\left(\frac{g_i^0(T)}{RT} + \ln(P) + \ln\frac{y_i + \lambda\Delta_i}{\bar{y} + \lambda\bar{\Delta}}\right) \quad (3.36)$$

To make sure that the new, corrected values $x_i^{'}$ are all positive, the distance traveled is limited to fractional amounts given by $\lambda\Delta_i$, using the largest possible value of λ that meets the required conditions [113, 114]:

- The function called the directional derivative is defined and exists:

$$\frac{dF(\lambda)}{d\lambda} = \sum_i \Delta_i\left(\frac{g_i^0(T)}{RT} + \ln(P) + \ln\frac{y_i + \lambda\Delta_i}{\bar{y} + \lambda\bar{\Delta}}\right) \quad (3.37)$$

- The directional derivative does not become positive (the minimum point is not passed).

Every new iteration begins with a different set of y_i, which changes the convex function $F(\lambda)$ defined by equation (3.36) and produces a new minimum. This leads to a new value of λ. After some number of iterations, λ will tend to approach the value of 1. When λ is close to 1, it means that the solution is near. The Lagrangian method and the lambda correction are repeated until either a predetermined error tolerance is reached or the maximum number of iterations has been reached.

3.5 Gaussian elimination with backward substitution

Gauss elimination is an algorithm for solving systems of linear equations. Given a system of n linear equations with n variables, the goal is to find values for the variables that simultaneously satisfy all the equations [115].

The algorithm works by manipulating the equations so that they are in a specific form, called triangular form, in which all the coefficients of the variables in the lower rows are zero. This is achieved through a series of elementary row operations, which do not change the solution of the system.

The elementary row operations that can be applied to the equations so as to transform a linear system into an equivalent one having the same solution but a triangular coefficient matrix are [116]:

- Interchanging two rows;
- Multiplying a row by a nonzero scalar;
- Replacing a row with a linear combination of itself and another row.

Once the equations are in triangular form, the solution can be found by back substitution, which is a method of solving the equations from bottom to top, starting with the last equation and working upwards.

The process of eliminating unknowns from equations one by one is called forward elimination. The process of finding the solution to a system of equations with a triangular matrix involves starting with the last component of the solution and working backward, substituting the values found into the remaining equations. This is known as backward substitution [115].

The Gaussian elimination for the case of an $n \times n$ linear system (with n equations and n unknowns). Written as a matrix equation, the system reads [116]:

$$\mathbf{A} \cdot \mathbf{x} = \mathbf{b} \quad (3.38)$$

and features the coefficient matrix $\mathbf{A} = [a_{ij}]_{nn}$, column vector $\mathbf{b} = [b_i]_n$ of the constant terms, and the column vector $\mathbf{x} = [x_i]_n$ of solution components.

The operations to be carried out on the matrices A and B at step $k = 1, ..., n$ of the forward elimination, the pivot row k is divided by the pivot $a_{kk}^{(k-1)}$ [116]:

$$\begin{cases} a_{kj}^{(k)} = a_{kj}^{(k-1)} / a_{kk}^{(k-1)}, & j = k+1, ..., n \\ b_{kj}^{(k)} = b_{kj}^{(k-1)} / a_{kk}^{(k-1)}, & j = 1, ..., m \end{cases} \quad (3.39)$$

while the non-pivot rows situated below the pivot row are reduced according to [116]:

$$\begin{cases} a_{ij}^{(k)} = a_{ij}^{(k-1)} - a_{ik}^{(k-1)} a_{kj}^{(k)}, & i = k+1, ..., n, \quad j = k+1, ..., n \\ b_{ij}^{(k)} = b_{ij}^{(k-1)} - a_{ik}^{(k-1)} b_{kj}^{(k)}, & i = k+1, ..., n, \quad j = 1, ..., m \end{cases} \quad (3.40)$$

The system takes the form [116]:

$$\begin{bmatrix} 1 & a_{12}^{(1)} & \dots & a_{1k}^{(1)} & a_{1k+1}^{(1)} & \dots & a_{1n}^{(1)} \\ 0 & 1 & \dots & a_{2k}^{(2)} & a_{2k+1}^{(2)} & \dots & a_{2n}^{(2)} \\ \vdots & \vdots & \ddots & \vdots & \vdots & & \vdots \\ 0 & 0 & \dots & 1 & a_{kk+1}^{(k)} & \dots & a_{kn}^{(k)} \\ 0 & 0 & \dots & 0 & 1 & \dots & a_{k+1n}^{(k+1)} \\ \vdots & \vdots & & \vdots & \vdots & \ddots & \vdots \\ 0 & 0 & \dots & 0 & 0 & \dots & 1 \end{bmatrix} \begin{bmatrix} x_1 \\ x_2 \\ \vdots \\ x_k \\ x_{k+1} \\ \vdots \\ x_n \end{bmatrix} = \begin{bmatrix} b_1^{(1)} \\ b_2^{(2)} \\ \vdots \\ b_k^{(k)} \\ b_{k+1}^{(k+1)} \\ \vdots \\ b_n^{(n)} \end{bmatrix} \tag{3.41}$$

The subsequent backward substitution operates based on the relations [116]:

$$\begin{cases} x_{nj} = b_{nj}^{(n)}, \quad j = 1, ..., m \\ x_{kj} = b_{kj}^{(k)} - \sum_{i=k+1}^{(n)} a_{ki}^{(k)} x_{ij}, \quad j = 1, ..., m, \quad k = n-1, ..., 1 \end{cases} \tag{3.42}$$

and yields the components of the solution matrix $\mathbf{X}$ column-wise (for each of the m simultaneous systems), in reversed order.

Gauss elimination is a popular method for solving systems of linear equations because it is relatively simple to implement and can be easily extended to handle systems with a large number of equations. However, it can be sensitive to round-off errors, especially for systems with poorly-conditioned (or ill-conditioned) matrices [117]. To mitigate this problem, it is common to use a variant of Gauss elimination called Gauss elimination with partial pivoting, which involves choosing the pivot element (the element on the diagonal of the matrix) in a way that reduces the occurrence of round-off errors [116]. Gauss elimination with partial pivoting is a variant of the Gauss elimination algorithm for solving systems of linear equations. It is similar to Gauss elimination, but it involves an additional step of choosing the pivot element (the element on the diagonal of the matrix) in a way that reduces the occurrence of round-off errors. By choosing the pivot element carefully, partial pivoting can help to reduce the occurrence of these errors and improve the numerical stability of the algorithm [117].

The basic idea of partial pivoting is to choose the pivot element as the element with the largest absolute value in the current column. To perform Gauss elimination with partial pivoting, the same steps as the regular Gauss elimination algorithm are executed, but the pivot element is chosen using partial pivoting before performing each elementary row operation. This involves finding, at the elimination step k, the maximum element $a_{lk}^{(k-1)}$ on column k, on and below the pivot row ($l \geq k$), and placing this element on the main diagonal (to become the actual pivot $a_{kk}^{(k-1)}$ by swapping rows k and l [116]. Then, the elementary row operation can be performed as usual. Once the equations are in triangular form, the system can be solved by back substitution as in the regular Gauss elimination algorithm.

3.6 Thermodynamic Data

This work uses thermodynamic data from the NASA Glenn Coefficients library, which includes information on the properties of various solid, liquid, and gaseous substances at temperatures from 200 to 20000 K [118]. The data in this library is presented in the form of coefficients for a seven-term equation for c_p^0/R that can be used to calculate thermodynamic functions, along with integration constants for h^0/RT and s^0/R. The coefficients were obtained using a computer program called PAC (Properties and Coefficients) developed by NASA Glenn. The resulting empirical equations for fitting thermodynamic functions are the following:

$$\frac{c_p^0(T)}{R} = a_1 T^{-2} + a_2 T^{-1} + a_3 + a_4 T + a_5 T^2 + a_6 T^3 + a_7 T^4 \quad (3.43)$$

Thus, enthalpy and entropy are obtained by integrating c_p^0 and c_p^0/T, respectively, with respect to T:

$$\frac{h^0(T)}{RT} = -a_1 T^{-2} + a_2 T^{-1} \ln T + a_3 + a_4 \frac{T}{2} + a_5 \frac{T^2}{3} + a_6 \frac{T^3}{4} + a_7 \frac{T^4}{5} + \frac{b_1}{T} \quad (3.44)$$

$$\frac{s^0(T)}{R} = -a_1 \frac{T^{-2}}{2} - a_2 T^{-1} + a_3 \ln T + a_4 T + a_5 \frac{T^2}{2} + a_6 \frac{T^3}{3} + a_7 \frac{T^4}{4} + b_2 \quad (3.45)$$

where b_1 and b_2 are integration constants.

The temperature range for fitting data for gases is divided into three intervals: 200 to 1000 K, 1000 to 6000 K, and for some simple molecules, 6000 to 20,000 K [118]. For nonionic gases, the temperature range for the fitted data is either 200 to 6000 K or 200 to 20,000 K. For ionic gases, the fitted data starts at 298.15 K. Only certain types of gases, such as the electron gas, monatomic species, and simple molecules like CO, CO2, N2, NO, and O+, have been fitted up to 20,000 K. There is a breakpoint in the fit for gases at 1000 K, and an additional breakpoint at 6000 K for gases fitted up to 20,000 K. The data presented are for substances in their standard state at a specific temperature, with the reference state being the thermodynamically stable state at 298.15 K [118]. For elements that are gases at 298.15 K and 1 bar, the reference state is considered gaseous for the entire temperature range. The enthalpy values for all reference elements in this thermodynamic library are set to zero at 298.15 K.

Furthermore, this thermodynamic data allows computing the term $g_i^0(T)$ in equation 3.8 for each species involved. This can be done with the following expression [119]:

$$\frac{g^0(T)}{RT} = \frac{1}{R}\left[\frac{g^0 - h^0(298.15)}{T}\right] + \frac{h_f^0(298.15)}{RT} \quad (3.46)$$

By definition, the Gibbs free energy is:

$$G = H - TS \quad (3.47)$$

Thus, the term in parentheses in equation 3.46 is:

$$\frac{g^0(T) - h^0(298.15)}{T} = -s^0(T) + \frac{h^0(T) - h^0(298.15)}{T} \quad (3.48)$$

The enthalpy of formation at $298.15K$ is also given, and for other temperatures can be calculated by:

$$h^0_{f,i} = h^0_i(T) - \sum \nu_j h^0_j(T) \quad (3.49)$$

3.7 Code implementation

The methodology presented in the previous sections can be implemented in several programming languages that have some ease with mathematical and algebraic operations. The most recommended and common programming languages would be Python, FORTRAN, C++, and Julia but there may be more. Generally, each one has its own advantages and disadvantages, but, in this case, it turns out to be the knowledge and experience in a certain language the decisive factor in choosing a programming language.

The suggested global implementation is shown in the flow-diagram in Fig. 3.2. As can be seen, there are two input values: equivalence ratio (ϕ) and pressure (p). For the reaction of one mol of hydrogen reacting with oxygen, the mol number of oxidant, a_{coef}, is given by:

$$a_{coef} = \frac{1}{2\phi} \quad (3.50)$$

When there is dissociation of combustion products, various chemical species appear in the equilibrium state. Thus, the solution of a chemical equilibrium problem or the determination of the adiabatic flame temperature requires defining of what chemical species are present in that equilibrium state. The species considered are based on Westbrook and Dryer [120], and Yetter et al. [121] works.

Model 1:

$$H_2 + a_{coef} O_2 \longmapsto n_{H_2O} H_2O + n_{O_2} O_2 + n_{H_2} H_2 + n_{OH} OH$$

Model 2:

$$H_2 + a_{coef} O_2 \longmapsto n_{H_2O} H_2O + n_{O_2} O_2 + n_{H_2} H_2 + n_{OH} OH + n_O O + n_H H$$

Model 3:

$$H_2 + a_{coef} O_2 \longmapsto n_{H_2O} H_2O + n_{O_2} O_2 + n_{H_2} H_2 + n_{OH} OH + n_O O + n_H H + n_{HO_2} HO_2 + n_{H_2O_2} H_2O_2$$

There are parameters that will have different values, depending on which model is being considered (see Fig. 3.2). Next, after all those inputs and initial parameters are defined, there is a loop that will calculate the adiabatic flame temperature. An initial range from T_{lb} to T_{ub}, such that $T_{lb} < T_{ad} < T_{up}$, should be given, so that the bisection method can be applied to compute T_{ad}, as already mentioned in previous sections. Inside this loop, the chemical equilibrium is necessary to calculate the enthalpy of reaction to solve Equation 3.5. To do this, a separate module, named "iterate Lagrange" in Fig. 3.2, is called in which the chemical equilibrium problem (Gibbs free energy minimization) will be solved. With this, the loop will proceed until error tolerance is satisfied or the maximum number of iterations is reached. The error tolerance is a value between zero and a value close to zero ($0 < \Delta H_R < error\ tolerance$), since it is intended that the enthalpy of reaction ΔH_R equals to zero as explained in section 3.1. Also, setting the enthalpy of reaction to zero is unreliable. Thus, in this case, a value of 10 ($0 < \Delta H_R < 10$) was sufficient so that the change in the temperature value was not at least more than 1 K with respect to the previous iteration. After all the calculations are done, the output is the adiabatic flame temperature and the equilibrium chemical composition for the given inputs of equivalence ratio and pressure for the selected model.

The suggested implementation of the methodology to solve the Gibbs free energy minimization problem is shown in Fig. 3.3. This separate module will be called by the main module that computes the adiabatic flame temperature and returns the chemical equilibrium composition for a given temperature. This occurs at the "iterate Lagrange" in the flow-diagram of the global implementation shown in Fig. 3.2. The module "Solve Lagrange" solves the system of equations 3.30 with the Gauss elimination method. There is a loop to iterate the chemical equilibrium mol solution until error tolerance is satisfied or the maximum number of iterations is reached. Inside this loop, there is a verification if all mol numbers are positive or negative. If all are positive, the program proceeds. Otherwise, it will call another separate module named "Lambda Correction" that will correct the solution to give all positive numbers, as described before.

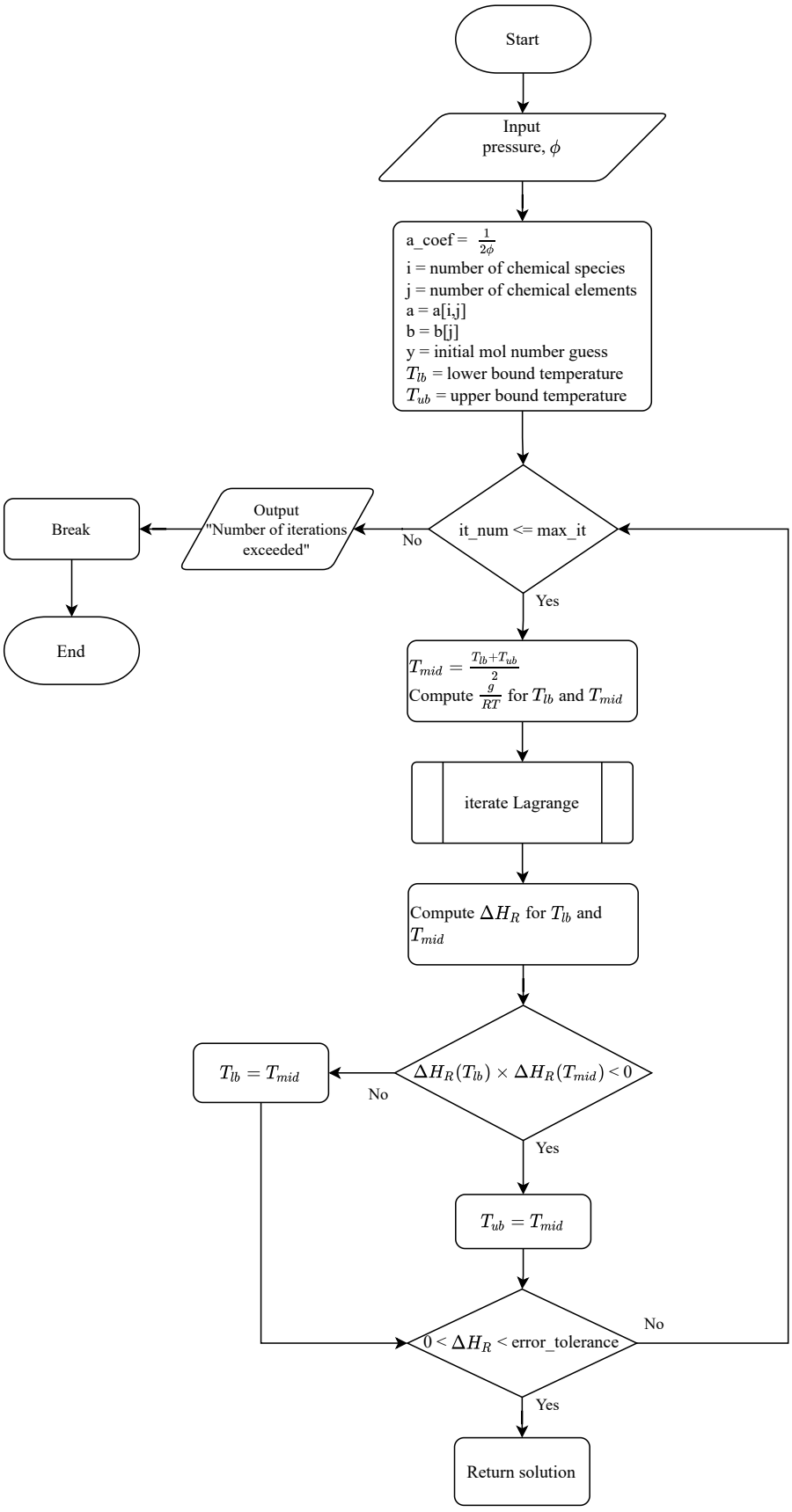

Figure 3.2: Flowchart of the global implementation.

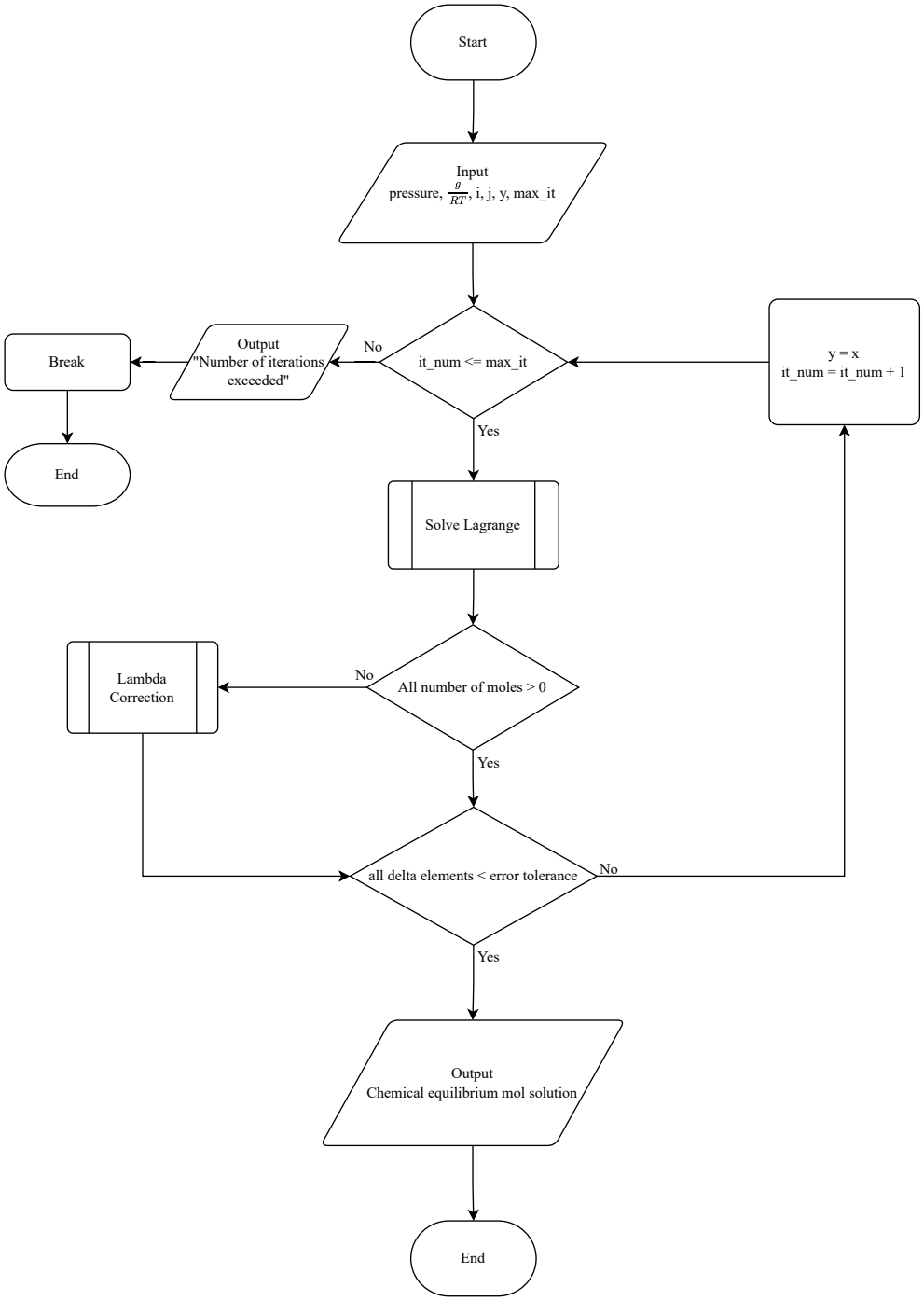

Figure 3.3: Flowchart of the Gibbs free energy minimization methodology.

3.8 Initial Guess

A feasible initial guess is needed so that the method can converge to a solution. This initial guess has to satisfy the atom number balance equation (i.e., the linear equality constraints of the minimization problem). There are possibly elaborate ways to obtain this initial guess for a more general problem, but for simplicity and probably for computing time, a more simple method is deduced based on the present problem. This means that for some other chemical reaction this method might not work.

Considering the reaction with 8 species

$$H_2 + a_{coef} O_2 \longmapsto n_{H_2O} H_2O + n_{O_2} O_2 + n_{H_2} H_2 + n_{OH} OH + n_O O + n_H H + n_{HO_2} HO_2 + n_{H_2O_2} H_2O_2$$

the atom balance system of equations is:

$$\begin{cases} 2n_{H_2O} + 2n_{H_2} + n_{OH} + n_H + n_{HO_2} + 2n_{H_2O_2} = 2 \\ n_{H_2O} + 2n_{O_2} + n_{OH} + 2n_{HO_2} + 2n_{H_2O_2} = 2a \end{cases} \tag{3.51}$$

Some *arbitrary* values will be attributed to 6 unknowns, leaving 2 unknowns to be determined with 2 equations. In matrix form, the problem is

$$\mathbf{A} \cdot \mathbf{x} = \mathbf{b} \tag{3.52}$$

where the vector $\mathbf{x}$ can be determined with the following

$$\mathbf{x} = \mathbf{A}^{-1} \cdot \mathbf{b} \tag{3.53}$$

The goal is to observe the system and see what are the two unknowns that facilitate the resolution of this specific problem. If n_{O_2} and n_{H_2} are set as the two unknowns it can be seen that each mass balance equation will have just one unknown allowing to solve them directly. Also, all the chemical reaction models have these two species in them, making it possible to always use these two unknowns for each model.

$$\begin{cases} 2n_{H_2} = 2 - 2n_{H2O} - n_{OH} + n_H + n_{HO2} - 2n_{H2O2} \\ 2n_{O_2} = 2a - n_{H2O} + n_{OH} + n_O - 2n_{HO2} - 2n_{H2O2} \end{cases} \tag{3.54}$$

Further, for each model:

$$\mathbf{A} = \begin{bmatrix} 0 & 2 \\ 2 & 0 \end{bmatrix} \tag{3.55}$$

The initial guess for the 6 variables should be such that either n_{H_2} or n_{O_2} do not result in

negative values. That is:

$$\begin{cases} 1 - n_{H2O} - \frac{1}{2}(n_{OH} + n_H + n_{HO2}) - n_{H2O2} > 0 \\ a - \frac{1}{2}(n_{H2O} + n_{OH} + n_O) - n_{HO2} - n_{H2O2} > 0 \end{cases} \tag{3.56}$$

The value of a depends on the equivalence ratio, ϕ, and as a range from 0.6 to 1.4 will be used, then the resulting a range is from 0.357 to 0.833. A little trial and error, the initial guesses can be:

$$n_{H2O} = 0.5$$

$$n_{OH} = 0.01$$

$$n_O = 0.1$$

$$n_H = 0.1$$

$$n_{HO2} = 0.01$$

$$n_{H2O2} = 0.01$$

For the models with 6 and 4 species, the procedure is identical, and the only difference is the number of species existent in each chemical reaction model.

Chapter 4

Results and discussion

For each model, the adiabatic flame temperature and the mol fractions at equilibrium composition, for each species, for the pressures of 1, 5, and 10 MPa were computed. These values are based on pressure from tables 2.2, 2.3, and 2.4. The lowest and highest pressure values represent subcritical and supercritical pressures with respect to the critical pressures of both hydrogen and oxygen, respectively. The pressure of 5 MPa represents the case in which the pressure is supercritical with respect to hydrogen but is at the critical point of oxygen. As the thermodynamic data is from 200K, the liquid phase of oxygen is not covered. Thus, the propellants were assumed to be at ambient temperature.

4.1 Adiabatic Flame Temperature Calculation Results

The results indicate that the adiabatic flame temperature ranges between 3000 to 4000 K (Figures 4.1, 4.2, 4.3) for the considered conditions.

The effect pressure has on adiabatic flame temperature can be seen. The adiabatic flame temperature increases with increasing pressure. This is explained by the fact that dissociation decreases with increasing pressure. That is, species that result from dissociation have their mol fractions decreased when pressure increases, which means that there are more reactants converted into species completely oxidized. Thus, this justifies the increase of adiabatic flame temperature with increasing pressure.

The adiabatic flame temperature is maximum for an equivalence ratio of approximately $\phi = 1.05$, that is, near stoichiometric mixture ($\phi = 1$), but just a little into the rich mixtures. This off-stoichiometric peaking of adiabatic flame temperature was studied by Law et al. [122]. They discovered that the occurrence of this phenomenon results from a decrease in the amount of heat released when the products are dissociated. The direction in which the heat release shifts is determined by the direction of the peak heat release and how the specific heat of the product mixture, per unit mass, varies based on the proportion of its elements. Both the combustion enthalpy and heat of reaction of products decrease for rich mixtures ($\phi > 1$). However, when ϕ increases from 1 to 1.05, the heat of reaction of products decreases more rapidly than the combustion enthalpy, which increases the adiabatic flame temperature. When ϕ increases to values greater than 1.05, the heat of reaction decreases slower than the combustion enthalpy, which justifies the decrease in combustion enthalpy.

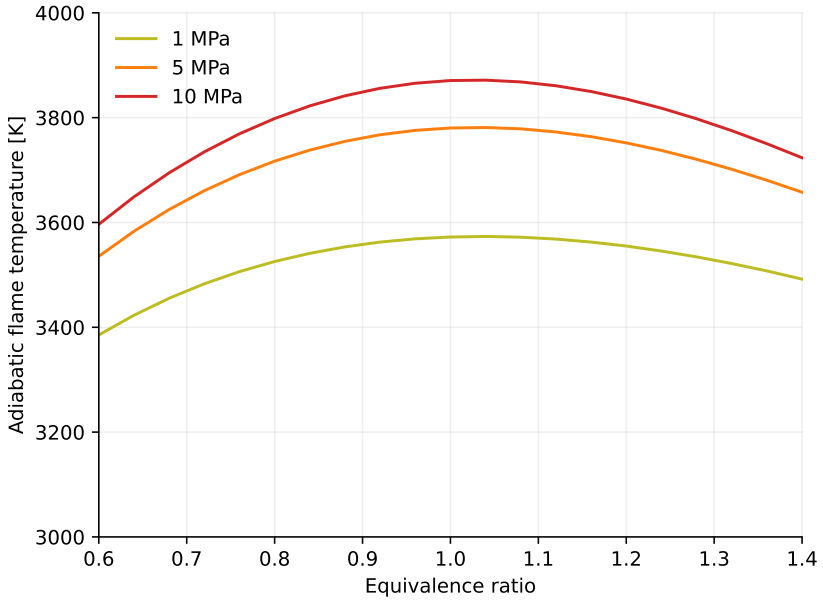

Figure 4.1: Adiabatic flame temperature as a function of equivalence ratio for model 1.

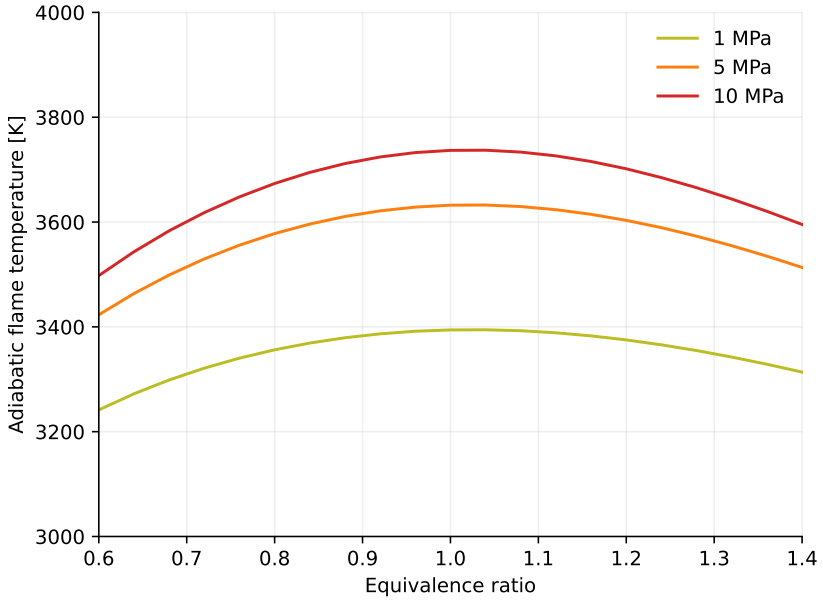

Figure 4.2: Adiabatic flame temperature as a function of equivalence ratio for model 2.

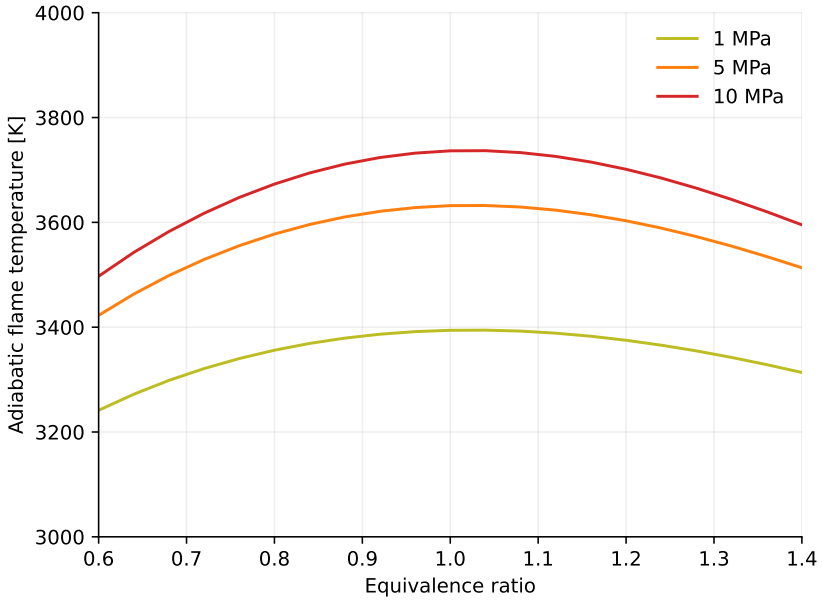

Figure 4.3: Adiabatic flame temperature as a function of equivalence ratio for model 3.

4.2 Equilibrium Chemical Composition Results

Figures 4.4, 4.5, and 4.6, show the mole fraction for each species as a function of the equivalence ratio for the pressures of 1, 5, and 10 MPa. For poor mixtures, there is excess oxygen, that is, species like O_2 and O, and for rich mixtures, there is excess hydrogen, that is, species like H_2 and H. Species like HO_2 and H_2O_2 have 10^{-5} magnitude order mole fractions, making it possible to ignore them for calculations without interference in the results. Furthermore, it can be observed that an increase in pressure raises the mole fraction of H_2O and lowers it for the other remaining species. This is in accordance with the fact that increasing pressure leads to higher adiabatic flame temperature, as there is less dissociation. Thus, when the values of the H_2O mole fraction are high, the adiabatic flame temperature will also take higher values so that the shape of both curves as a function of the equivalence ratio is similar.

Also, in these figures, it is seen that the extent of dissociation is greater on the lean side, and thus the peaking of the adiabatic flame temperature occurs on the rich side, as suggested in [122].

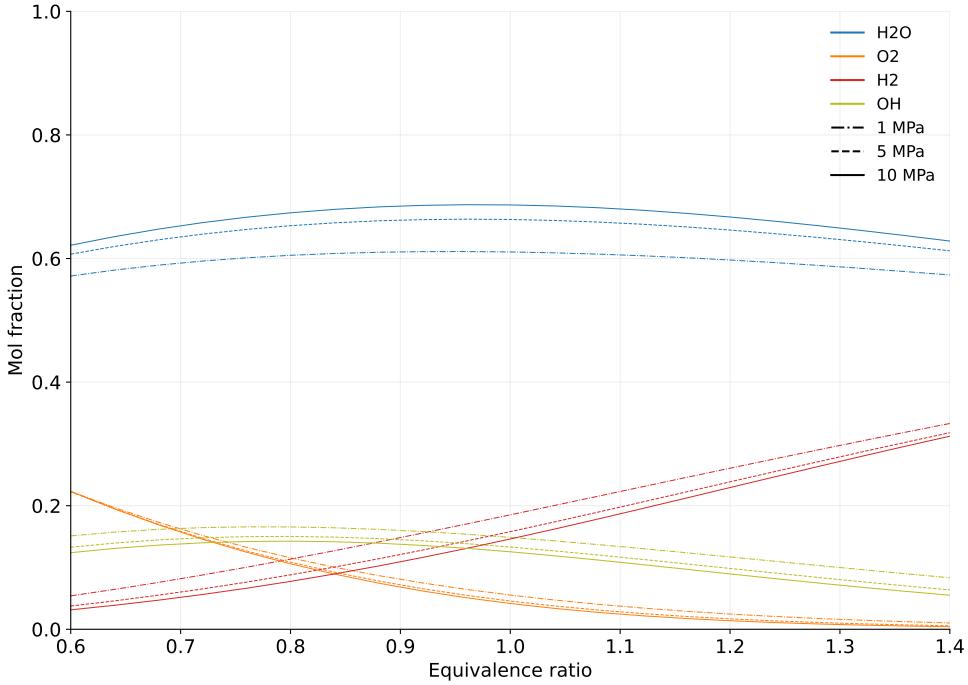

Figure 4.4: Mol fractions as a function of equivalence ratio for model 1.

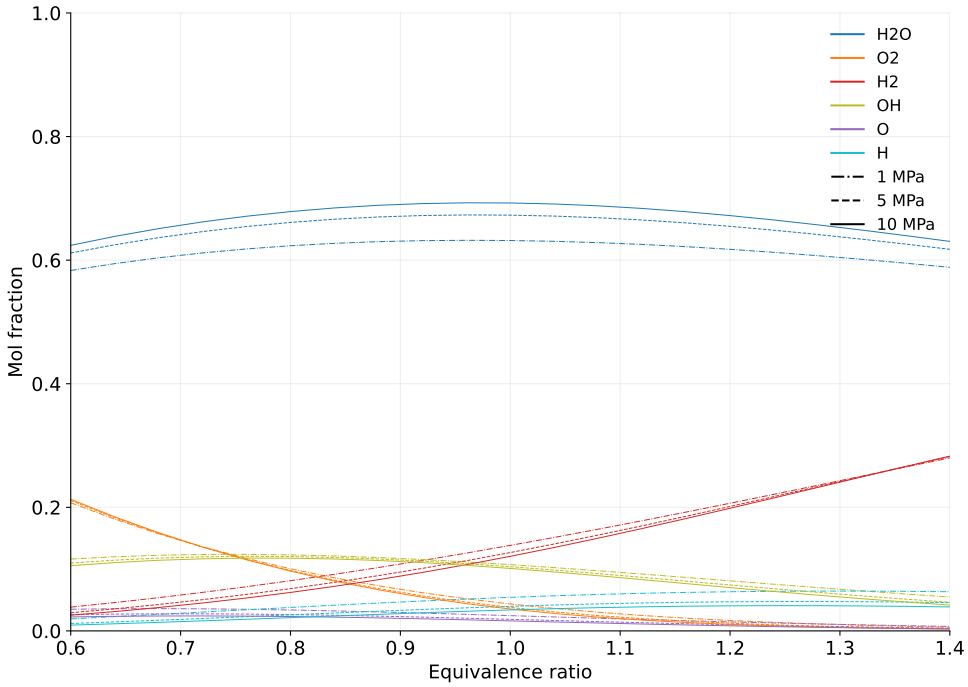

Figure 4.5: Mol fractions as a function of equivalence ratio for model 2.

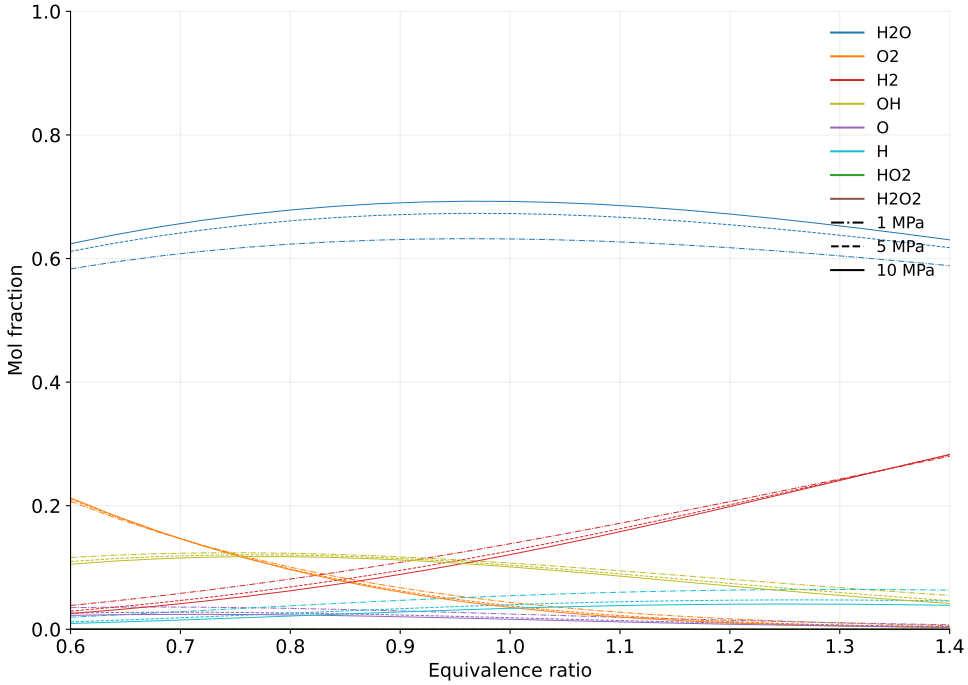

Figure 4.6: Mol fractions as a function of equivalence ratio for model 3.

4.3 Execution time results

The Python programming language was utilized to implement the methodology presented in the previous chapter. The execution time of the code to plot for each model the adiabatic flame temperature and chemical equilibrium mol fractions from the previous figures are shown in table 4.1. Also, the execution time of the code to compute the adiabatic flame temperature and chemical equilibrium mol fractions for a single combination of equivalence ratio and pressure was always less than one second, using a computer with a Intel(R) Core(TM) i5-6200U CPU and 6GB of RAM. It should be noted that chosen programming language can have a significant impact on the execution time. Moreover, the experience of the programmer can have a great impact on the ”quality” of the scripts and, thus, on the execution times.

Table 4.1: Execution times.

Model	Time to plot Tad [s]	Time to plot mol fractions [s]
Model 1	32	69
Model 2	38	91
Model 3	51	124

Overall the resulting execution times are acceptable, but there might be room for improvement.

Chapter 5

Conclusions and Future Work

The adiabatic flame temperature of the combustion reaction between hydrogen and oxygen was calculated, considering the dissociation of combustion products. This has considerable relevance in liquid propellant rocket engines that use the combination of liquid oxygen and liquid hydrogen as propellants. Moreover, it was also of interest to observe the chemical equilibrium composition at the computed adiabatic flame temperature. Three combustion reactions were used, each with a different number of chemical species to investigate the effect that adding species would have on the value of the adiabatic flame temperature.

Several methodologies, such as bisection and minimization methods, Gauss elimination, and others, were necessary to calculate the adiabatic flame temperature but also to solve the subproblems originated by this calculation, like the Gibbs free energy minimization problem. Also, a thermodynamic database with an extensive temperature range of application to compute the thermodynamic properties of individual species was required. An implementation of the methodology developed to compute the adiabatic flame temperature, and the chemical equilibrium composition was also proposed.

On a concluding note, the methodology presented in this work and the results it can provide creates a tool that can help a preliminary design phase of an LRE, specifically, in this case, one that uses liquid oxygen and liquid hydrogen as propellants. However, only a small part of that preliminary design phase can be made with this tool. Or in other words, it would be just the beginning of a tool capable of doing that preliminary design phase. Thus, an extension of this work can be performed as future work. This extension would include a methodology that would enable prediction or verify various propulsive parameters such as chamber pressure, specific impulse, thrust, and mass flow. Also, it could analyze and perform calculations related to the nozzle and help with the engine cycle selection. Moreover, the ability to perform optimization and to provide the impact of specific parameters on a design would be very important. Lastly, the results of this work provide an initial study of the characteristics of the combustion reaction between oxygen and hydrogen. This is the first step that the AEROG research group is looking for in order to be able to include the modeling of combustion in their numerical simulations. This way, a significant step forward can be taken regarding research on numerical modeling of LRE injection and combustion.

Bibliography

[1] Sutton, G. P., *History of Liquid Propellant Rocket Engines*, American Institute of Aeronautics and Astronautics, 2006. 1, 5, 13

[2] Palaszewski, B. A., Meyer, M. L., Johnson, L., Goebel, D. M., White, H., and Coote, D. J., "In-Space Chemical Propulsion System Roadmap," *Chemical Rocket Propulsion*, Springer International Publishing, aug 2016, pp. 655–671. 1

[3] Ito, J. I., "Propellant Injection Systems and Processes," *Liquid Rocket Thrust Chambers: Aspects of Modeling, Analysis,and Design*, Vol. 200, American Institute of Aeronautics and Astronautics, jan 2004, pp. 1–18. 1

[4] Barata, J. M. M., Gokalp, I., and Silva, A. R. R., "Numerical Study of Cryogenic Jets Under Supercritical Conditions," *Journal of Propulsion and Power*, Vol. 19, No. 1, jan 2003, pp. 142–147. 2

[5] Antunes, E. L. S. F., Silva, A. R. R., and Barata, J. M. M., "RANS Modeling of Transcritical and Supercritical Nitrogen Jets," *53rd AIAA Aerospace Sciences Meeting*, American Institute of Aeronautics and Astronautics, Kissimmee, Florida, jan 2015. 2, 19

[6] Antunes, E., Silva, A., and Barata, J., "Variable Density Approach for Modeling of Transcritical and Supercritical Jets," *Journal of Engineering and Applied Sciences*, Vol. 12, No. 20, Nov. 2017, pp. 5147–5159. 2

[7] Antunes, E., Silva, A., and Barata, J., "Modelling of transcritical and supercritical nitrogen jets," *Combustion Engines*, Vol. 169, No. 2, may 2017, pp. 125–132. 2

[8] Magalhães, L., Carvalho, F., Silva, A., and Barata, J., "Turbulence Modeling Insights into Supercritical Nitrogen Mixing Layers," *Energies*, Vol. 13, No. 7, apr 2020, pp. 1586. 2, 19

[9] Magalhães, L., Carvalho, F., Silva, A., and Barata, J., "Turbulence Quantification in Supercritical Nitrogen Injection: An Analysis of Turbulence Models," *KnE Engineering*, jun 2020. 2

[10] Magalhaes, L. B., Silva, A. R., and Barata, J. M., "The Role of Injector Heat Transfer in Supercritical Injection Phenomena," *AIAA Propulsion and Energy 2020 Forum*, American Institute of Aeronautics and Astronautics, aug 2020. 2

[11] Magalhães, L. B., Silva, A. R., and Barata, J. M., "Contribution to the physical description of supercritical cold flow injection: The case of nitrogen," *Acta Astronautica*,

Vol. 190, jan 2022, pp. 251–260. 2

[12] Magalhães, L. B., Silva, A. R. R., and Barata, J. M. M., "Supercritical Injection Modeling by an Incompressible but Variable Density Approach," *Aerospace*, Vol. 10, No. 2, jan 2023, pp. 114. 2

[13] Magalhães, L. B., Silva, A. R. R., and Barata, J. M. M., "Temperature Field Validation on Supercritical Coaxial Injection," *9th European Conference for Aerospace Sciences (EUCASS)*, Lille, France, July 2022. 2

[14] Sutton, G. P. and Biblarz, O., *Rocket Propulsion Elements*, Wiley, 9th ed., 2016. 2, 5, 7, 8, 9, 10, 11, 12, 13

[15] Heister, S. D., Anderson, W. E., Pourpoint, T. L., and Cassady, R. J., *Rocket Propulsion*, Cambridge University Press, 1st ed., 2019. 5, 13, 14

[16] Mishra, D. P., *Fundamentals of Rocket Propulsion*, Taylor & Francis Group, 1st ed., 2017. 5

[17] Anderson Jr., J. D., *Introduction to Flight*, McGraw Hill, 8th ed., 2015. 6, 7, 8

[18] Haidn, O. J., "Advanced rocket engines," *Advances on propulsion Technology for High-Speed Aircraft*, Vol. 1, 2008, pp. 1–40, Educational Notes RTO-EN-AVT-150. 9, 11

[19] Ernst, R. R. L., *Liquid Rocket Analysis (LiRA) Development of a Liquid Bi-Propellant Rocket Engine Design, Analysis and Optimization Tool*, Master's thesis, Delft University of Technology, 2014. 10, 11

[20] Kim, Y. and Moon, Y. W., "Optimization and Application of Cryogenic/Thermal Insulation Design for a Liquid-propellant Rocket Engine," 2019. 11

[21] Burow, R., Just, D., Adamczyk, A., Jagels, C., Milke, A., Wendt, C., and Kneistler, H., "Thermal Control of the Cryogenic Upper Stage of Ariane 6," *49th International Conference on Environmental Systems*, Boston, Massachusetts, USA, July 2019. 11

[22] Hopkins Jr., J., Hopkins, J., and Isakowitz, S., *International Reference Guide to Space Launch Systems*, American Institute of Aeronautics and Astronautics, Inc., 4th ed., 2004. 12, 13

[23] Huzel, D. K. and Huang, D. H., *Modern Engineering for Design of Liquid-Propellant Rocket Engines (Progress in Astronautics and Aeronautics)*, AIAA (American Institute of Aeronautics & Astronautics), 1992. 12, 13

[24] Cai, G., Jin, P., Yang, L., Du, Z., and Xu, K., "Experimental and Numerical Investigation of Gas-Gas Injectors for Full Flow Stage Combustion Cycle Engine," *41st AIAA/ASME/SAE/ASEE Joint Propulsion Conference & Exhibit*, American Institute of Aeronautics and Astronautics, jul 2005. 12, 13

[25] Davis, J. and Campbell, R., "Advantages of a full-flow staged combustion cycle engine system," *33rd Joint Propulsion Conference and Exhibit*, American Institute of Aeronautics and Astronautics, jul 1997. 12, 13

[26] Wade, M., "Encyclopedia Astronautica," `http://www.astronautix.com`, Last accessed on 2022-09-05. 12, 13

[27] Brossel, P., Caisso, P., Illig, M., and Margat, T., "Development Status of the Vulcain 2 Engine," *38th AIAA/ASME/SAE/ASEE Joint Propulsion Conference & Exhibit*, American Institute of Aeronautics and Astronautics, jul 2002. 12

[28] Wang, W., Zheng, D., and Qiao, G., "Development Status of the Cryogenic Oxygen/Hydrogen YF-77 Engine for Long-March 5," *64rd International Astronautical Congress*, International Astronautical Federation, 2013. 12

[29] "HM-7 and HM-7B Rocket Engine - Thrust Chamber," `https://web.archive.org/web/20120508062948/http://cs.astrium.eads.net/sp/launcher-propulsion/rocket-engines/hm7b-rocket-engine.html`, Last accessed on 2021-11-17. 13

[30] Sippel, M., Herbertz, A., Burkhardt, H., Imoto, T., Haeseler, D., and Götz, A., "Studies on Expander Bleed Cycle Engines for Launchers," *39th AIAA/ASME/SAE/ASEE Joint Propulsion Conference and Exhibit*, American Institute of Aeronautics and Astronautics, jun 2003. 13

[31] Allison, T., "JANAF Thermochemical Tables, NIST Standard Reference Database 13," 1996. 13

[32] Lefebvre, A. H. and McDonell, V. G., *Atomization and sprays*, Taylor & Francis, CRC Press, Boca Raton, 2017. 13

[33] Hulka, J. and Hutt, J. J., "Instability Phenomenology and Case Studies: Instability Phenomena in Liquid Oxygen/Hydrogen Propellant Rocket Engines," *Liquid Rocket Engine Combustion Instability*, American Institute of Aeronautics and Astronautics, jan 1995, pp. 39–71. 13

[34] Banuti, D., *Thermodynamic Analysis and Numerical Modeling of Supercritical Injection*, Ph.D. thesis, Faculty of Aerospace Engineering and Geodesy of the Universität Stuttgart, 2014. 15, 16, 19, 21

[35] Anderson, W. E. and Yang, V., *Liquid Rocket Engine Combustion Instability*, Vol. 169, American Institute of Aeronautics and Astronautics, jan 1995. 15

[36] Candel, S., Herding, G., Synder, R., Scouflaire, P., Rolon, C., Vingert, L., Habiballah, M., Grisch, F., Pealat, M., Bouchardy, P., Stepowski, D., Cessou, A., and Colin, P., "Experimental Investigation of Shear Coaxial Cryogenic Jet Flames," *Journal of Propulsion and Power*, Vol. 14, No. 5, sep 1998, pp. 826–834. 15, 30, 33

[37] Snyder, R., Herding, G., Rolon, J. C., and Candel, S., "Analysis of Flame Patterns in Cryogenic Propellant Combustion," *Combustion Science and Technology*, Vol. 124, No. 1-6, mar 1997, pp. 331–370. 15

[38] Smith, J., Klimenko, D., Clauss, W., and Mayer, W., "Supercritical LOX/Hydrogen Rocket Combustion Investigations Using Optical Diagnostics," *38th AIAA/ASME/SAE/ASEE Joint Propulsion Conference & Exhibit*, American Institute of Aeronautics and Astronautics, jul 2002. 15, 30, 33

[39] Woodward, R., Pal, S., Farhangi, S., and Santoro, R., "LOX/GH2 Shear Coaxial Injector Atomization Studies at Large Momentum Flux Ratios," *42nd AIAA/ASME/SAE/ASEE Joint Propulsion Conference & Exhibit*, American Institute of Aeronautics and Astronautics, jul 2006. 15

[40] Mayer, W. and Tamura, H., "Propellant injection in a liquid oxygen/gaseous hydrogen rocket engine," *Journal of Propulsion and Power*, Vol. 12, No. 6, nov 1996, pp. 1137–1147. 16, 17, 21, 29, 33

[41] Kendrick, D., "Effects of a recess on cryogenic flame stabilization," *Combustion and Flame*, Vol. 118, No. 3, aug 1999, pp. 327–339. 16, 30, 33

[42] Turns, S. R., *Thermodynamics*, Cambridge University Press, 2006. 16

[43] Oefelein, J. C., "Thermophysical characteristics of shear-coaxial LOX–H2 flames at supercritical pressure," *Proceedings of the Combustion Institute*, Vol. 30, No. 2, jan 2005, pp. 2929–2937. 16

[44] Oschwald, M., Smith, J. J., Branam, R., Hussong, J., Schik, A., Chehroudi, B., and Talley, D., "Injection of Fluids Into Supercritical Environments," *Combustion Science and Technology*, Vol. 178, No. 1-3, jan 2006, pp. 49–100. 16, 22, 27, 28

[45] Oefelein, J. C., "Mixing and Combustion of Cryogenic Oxygen-Hydrogen Shear-Coaxial Jet Flames at Supercritical Pressure," *Combustion Science and Technology*, Vol. 178, No. 1-3, jan 2006, pp. 229–252. 16, 17, 27

[46] Candel, S., Juniper, M., Singla, G., Scouflaire, P., and Rolon, C., "Structure and Dynamics of Cryogenic Flames at Supercritical Pressure," *Combustion Science and Technology*, Vol. 178, No. 1-3, jan 2006, pp. 161–192. 16, 17, 26, 30, 31, 33

[47] Linstrom, P., "NIST Chemistry WebBook, NIST Standard Reference Database 69," 1997. 18, 19, 20, 21

[48] Bellan, J., "Supercritical (and subcritical) fluid behavior and modeling: drops, streams, shear and mixing layers, jets and sprays," *Progress in Energy and Combustion Science*, Vol. 26, No. 4-6, aug 2000, pp. 329–366. 19

[49] Yang, V., "Modeling of supercritical vaporization, mixing, and combustion processes in liquid-fueled propulsion systems," *Proceedings of the Combustion Institute*, Vol. 28, No. 1, jan 2000, pp. 925–942. 19

[50] Banuti, D. T., "Crossing the Widom-line – Supercritical pseudo-boiling," *The Journal of Supercritical Fluids*, Vol. 98, mar 2015, pp. 12–16. 19

[51] Mayer, W. O. H., Ivancic, B., Schik, A., and Hornung, U., "Propellant Atomization and Ignition Phenomena in Liquid Oxygen/Gaseous Hydrogen Rocket Combustors," *Journal of Propulsion and Power*, Vol. 17, No. 4, jul 2001, pp. 794–799. 21, 22, 23, 24, 33

[52] Banuti, D., Raju, M., Ma, P. C., Ihme, M., and Hickey, J.-P., "Seven questions about supercritical fluids - towards a new fluid state diagram," *55th AIAA Aerospace Sciences Meeting*, American Institute of Aeronautics and Astronautics, jan 2017. 21

[53] Banuti, D., "The Latent Heat of Supercritical Fluids," *Periodica Polytechnica Chemical Engineering*, Vol. 63, No. 2, jan 2019, pp. 270–275. 21

[54] Banuti, D. T., Raju, M., and Ihme, M., "Similarity law for Widom lines and coexistence lines," *Physical Review E*, Vol. 95, No. 5, may 2017, pp. 052120. 21

[55] Oefelein, J. C. and Yang, V., "Modeling High-Pressure Mixing and Combustion Processes in Liquid Rocket Engines," *Journal of Propulsion and Power*, Vol. 14, No. 5, sep 1998, pp. 843–857. 21

[56] Mayer, W. O. H., Schik, A. H. A., Vielle, B., Chauveau, C., Gokalp, I., Talley, D. G., and Woodward, R. D., "Atomization and Breakup of Cryogenic Propellants Under High-Pressure Subcritical and Supercritical Conditions," *Journal of Propulsion and Power*, Vol. 14, No. 5, sep 1998, pp. 835–842. 22

[57] Mayer, W. O. H. and Smith, J. J., "Fundamentals of Supercritical Mixing and Combus-

tion of Cryogenic Propellants," *Liquid Rocket Thrust Chambers*, American Institute of Aeronautics and Astronautics, jan 2004, pp. 339–367. 22, 23, 25

[58] Chehroudi, B., Talley, D., and Coy, E., "Visual characteristics and initial growth rates of round cryogenic jets at subcritical and supercritical pressures," *Physics of Fluids*, Vol. 14, No. 2, feb 2002, pp. 850–861. 22

[59] Chehroudi, B. and Talley, D., "Interaction of acoustic waves with a cryogenic nitrogen jet at sub- and supercritical pressures," *40th AIAA Aerospace Sciences Meeting & Exhibit*, American Institute of Aeronautics and Astronautics, jan 2002. 22

[60] Oschwald, M. and Schik, A., "Supercritical nitrogen free jet investigated by spontaneous Raman scattering," *Experiments in Fluids*, Vol. 27, No. 6, nov 1999, pp. 497–506. 22, 25

[61] Chehroudi, B., Cohn, R., Talley, D., and Badakhshan, A., "Raman scattering measurements in the initial region of sub- and supercritical jets," *36th AIAA/ASME/SAE/ASEE Joint Propulsion Conference and Exhibit*, American Institute of Aeronautics and Astronautics, jul 2000. 22

[62] Mayer, W., Telaar, J., Branam, R., Schneider, G., and Hussong, J., "Raman Measurements of Cryogenic Injection at Supercritical Pressure," *Heat and Mass Transfer*, Vol. 39, No. 8-9, jul 2002, pp. 709–719. 22, 25

[63] Branam, R. and Mayer, W., "Characterization of Cryogenic Injection at Supercritical Pressure," *Journal of Propulsion and Power*, Vol. 19, No. 3, may 2003, pp. 342–355. 25

[64] Oschwald, M., Schik, A., Klar, M., and Mayer, W., "Investigation of coaxial LN2/GH2-injection at supercritical pressure by spontaneous Raman scattering," *35th Joint Propulsion Conference and Exhibit*, American Institute of Aeronautics and Astronautics, jun 1999. 25

[65] Habiballah, M., Orain, M., Grisch, F., Vingert, L., and Gicquel, P., "Experimental Studies of High-Pressure Cryogenic Flames on the Mascotte Facility," *Combustion Science and Technology*, Vol. 178, No. 1-3, jan 2006, pp. 101–128. 25, 26, 33

[66] "Test Case RCM-3 Mascotte Single Injector -60 Bar," *2nd International Workshop on Rocket Combustion Modeling: Atomization, Combustion and Heat Transfer*, Lampoldshausen, Germany, March 2001. 26

[67] Vingert, L., Habiballah, M., and Traineau, J. C., "Mascotte a Research Test facility for High pressure Combustion of Cryogenic Propellants," *3rd European Conference on*

Space Transportation Systems, Paris, France, 1999. 25

[68] Marshall, W., Pal, S., Woodward, R., and Santoro, R., "Benchmark Wall Heat Flux Data for a GO2/GH2 Single Element Combustor," *41st AIAA/ASME/SAE/ASEE Joint Propulsion Conference & Exhibit*, American Institute of Aeronautics and Astronautics, jul 2005. 26, 31, 33

[69] Knab, O., Riedmann, H., Ivancic, B., Höglauer, C., Frey, M., and Aichner, T., "Consequences of modeling demands on numerical rocket thrust chamber flow simulation tools," *Progress in Propulsion Physics – Volume 11*, EDP Sciences, 2019. 26

[70] Masquelet, M. and Menon, S., "Large-Eddy Simulation of Flame-Turbulence Interactions in a Shear Coaxial Injector," *Journal of Propulsion and Power*, Vol. 26, No. 5, sep 2010, pp. 924–935. 26

[71] Tucker, P., Menon, S., Merkle, C., Oefelein, J., and Yang, V., "An Approach to Improved Credibility of CFD Calculations for Rocket Injector Design," *43rd AIAA/ASME/SAE/ASEE Joint Propulsion Conference & Exhibit*, American Institute of Aeronautics and Astronautics, jul 2007. 27

[72] Lechtenberg, A. and Gerlinger, P. M., "Numerical Investigation of Combustion Instabilities in a Rocket Combustion Chamber with Supercritical Injection Using a Hybrid RANS/LES Method," *AIAA Scitech 2020 Forum*, American Institute of Aeronautics and Astronautics, jan 2020. 27, 28

[73] Martin, J., Armbruster, W., Stützer, R., General, S., Knapp, B., Suslov, D., and Hardi, J., "Flame characteristics of a high-pressure LOX/H2 rocket combustor with large optical access," *Case Studies in Thermal Engineering*, Vol. 28, dec 2021, pp. 101546. 28, 29, 32, 33

[74] Mayer, W., Schik, A., Schäffler, M., and Tamura, H., "Injection and Mixing Processes in High-Pressure Liquid Oxygen/Gaseous Hydrogen Rocket Combustors," *Journal of Propulsion and Power*, Vol. 16, No. 5, sep 2000, pp. 823–828. 30, 33

[75] Juniper, M., Tripathi, A., Scouflaire, P., Rolon, J. C., and Candel, S., "Structure of cryogenic flames at elevated pressures," *Proceedings of the Combustion Institute*, Vol. 28, No. 1, jan 2000, pp. 1103–1109. 30, 33

[76] Ivancic, B. and Mayer, W., "Time- and Length Scales of Combustion in Liquid Rocket Thrust Chambers," *Journal of Propulsion and Power*, Vol. 18, No. 2, mar 2002, pp. 247–253. 30, 33

[77] Conley, A., Vaidyanathan, A., and Segal, C., "Heat Flux Measurements for a GO2/GH2

Single-Element, Shear Injector," *Journal of Spacecraft and Rockets*, Vol. 44, No. 3, may 2007, pp. 633–639. 31, 33

[78] Smith, J. J., Schneider, G., Suslov, D., Oschwald, M., and Haidn, O., "Steady-state high pressure LOx/H2 rocket engine combustion," *Aerospace Science and Technology*, Vol. 11, No. 1, jan 2007, pp. 39–47. 31, 33

[79] Nunome, Y., Takahashi, M., Kumakawa, A., Miyazaki, K., Yoshida, S., and Onga, T., "High-Frequency Flame Oscillation Observed at a Coaxial LOX/LH2 Injector Element," *44th AIAA/ASME/SAE/ASEE Joint Propulsion Conference & Exhibit*, American Institute of Aeronautics and Astronautics, jul 2008. 31, 33

[80] Locke, J., Pal, S., Woodward, R., and Santoro, R., "High Speed Visualization of LOX/GH2 Rocket Injector Flowfield: Hot-Fire and Cold-Flow Experiments," *46th AIAA/ASME/SAE/ASEE Joint Propulsion Conference & Exhibit*, American Institute of Aeronautics and Astronautics, jul 2010. 31, 33

[81] Hardi, J. S., Beinke, S. K., Oschwald, M., and Dally, B. B., "Coupling of Cryogenic Oxygen–Hydrogen Flames to Longitudinal and Transverse Acoustic Instabilities," *Journal of Propulsion and Power*, Vol. 30, No. 4, jul 2014, pp. 991–1004. 31

[82] Roa, M. and Talley, D. G., "Wave Dynamic Mechanisms in Coaxial Hydrogen/Liquid-Oxygen Jet Flames," *Journal of Propulsion and Power*, Vol. 35, No. 2, mar 2019, pp. 369–381. 31, 33

[83] Suslov, D. I., Hardi, J. S., and Oschwald, M., "Full-length visualisation of liquid oxygen disintegration in a single injector sub-scale rocket combustor," *Aerospace Science and Technology*, Vol. 86, mar 2019, pp. 444–454. 32, 33

[84] Armbruster, W., Hardi, J. S., Suslov, D., and Oschwald, M., "Injector-Driven Flame Dynamics in a High-Pressure Multi-Element Oxygen–Hydrogen Rocket Thrust Chamber," *Journal of Propulsion and Power*, Vol. 35, No. 3, may 2019, pp. 632–644. 32, 33

[85] Hardi, J. S., Traudt, T., Bombardieri, C., Börner, M., Beinke, S. K., Armbruster, W., Blanco, P. N., Tonti, F., Suslov, D., Dally, B., and Oschwald, M., "Combustion dynamics in cryogenic rocket engines: Research programme at DLR Lampoldshausen," *Acta Astronautica*, Vol. 147, jun 2018, pp. 251–258. 33

[86] Rakopoulos, C. D., Hountalas, D. T., Tzanos, E. I., and Taklis, G. N., "A fast algorithm for calculating the composition of diesel combustion products using 11 species chemical equilibrium scheme," *Advances in Engineering Software*, Vol. 19, No. 2, jan 1994, pp. 109–119. 34

[87] Rashidi, M., "Calculation of equilibrium composition in combustion products," *Applied Thermal Engineering*, Vol. 18, No. 3-4, mar 1998, pp. 103–109. 34

[88] Coelho, P. and Costa, M., *Combustão*, Orion, 2007. 34, 37, 38

[89] Meintjes, K. and Morgan, A. P., "A methodology for solving chemical equilibrium systems," *Applied Mathematics and Computation*, Vol. 22, No. 4, jun 1987, pp. 333–361. 34

[90] Jarungthammachote, S., "Simplified model for estimations of combustion products, adiabatic flame temperature and properties of burned gas," *Thermal Science and Engineering Progress*, Vol. 17, jun 2020, pp. 100393. 34

[91] Kayadelen, H. K., "A multi-featured model for estimation of thermodynamic properties, adiabatic flame temperature and equilibrium combustion products of fuels, fuel blends, surrogates and fuel additives," *Energy*, Vol. 143, jan 2018, pp. 241–256. 34

[92] Gordon, S. and McBride, B. J., "Computer program for calculation of complex chemical equilibrium compositions with applications I. analysis," *NASA Report NASA RP-1311*, NASA, Washington, D.C.: NASA Lewis Research Center, Oct. 1994. 34, 35, 42

[93] Lwin, Y., "Chemical Equilibrium by Gibbs Energy Minimization on Spreadsheets," *International Journal of Engineering Education*, Vol. 16, Jan. 2000. 34

[94] Lilley, D., "Adiabatic Flame Temperature Calculation," *1st International Energy Conversion Engineering Conference (IECEC)*, American Institute of Aeronautics and Astronautics, jun 2003. 34

[95] Lilley, D., "Adiabatic Flame Temperature Calculation: A Simple Approach for General CHONS Fuels," *42nd AIAA Aerospace Sciences Meeting and Exhibit*, American Institute of Aeronautics and Astronautics, jan 2004. 34

[96] Rossi, C. C. R. S., Cardozo-Filho, L., and Guirardello, R., "Gibbs free energy minimization for the calculation of chemical and phase equilibrium using linear programming," *Fluid Phase Equilibria*, Vol. 278, No. 1-2, apr 2009, pp. 117–128. 34

[97] Gonçalves, R., Ferrão, L., Rocha, R., Machado, F., Iha, K., and Rocco, J. A., "Kinetic Simulation of Hydrogen Combustion in a Homogeneous Reactor," *46th AIAA/ASME/SAE/ASEE Joint Propulsion Conference & Exhibit*, American Institute of Aeronautics and Astronautics, jul 2010. 34

[98] Gonçalves, R., Iha, K., and Rocco, J. A. F., "Detailed Study of Hydrogen Combustion in Homogeneous Reactor," *48th AIAA/ASME/SAE/ASEE Joint Propulsion Conference*

& Exhibit, American Institute of Aeronautics and Astronautics, jul 2012. 34

[99] Shimizu, K., Hibi, A., Koshi, M., Morii, Y., and Tsuboi, N., "Updated Kinetic Mechanism for High-Pressure Hydrogen Combustion," *Journal of Propulsion and Power*, Vol. 27, No. 2, mar 2011, pp. 383–395. 34

[100] Gordon, S. and McBride, B. J., "Computer Program for Calculation of Complex Chemical Equilibrium Compositions, Rocket Performance, Incident and Reflected Shocks, and Chapman-Jouguet Detonations," *NASA SP-273*, NASA, Washington, D.C.: NASA Lewis Research Center, 1976. 35

[101] McBride, B. J. and Gordon, S., "Thermodynamic data for fifty reference elements," *NASA TP-3287*, 1993. 35

[102] Gordon, S. and McBride, B. J., "Computer program for calculation of complex chemical equilibrium compositions and applications II. User's manual and program description," *NASA Report NASA RP-1311-P2*, NASA, Washington, D.C.: NASA Lewis Research Center, June 1996. 35

[103] McBride, B. J. and Gordon, S., "Computer program for calculating and fitting thermodynamic functions," *NASA RP-1271*, 1992. 35

[104] McBride, B. J. and Gordon, S., "Coefficients for calculating thermodynamic and transport properties of individual species," *NASA TM-4513*, 1993. 35

[105] Gordon, S., McBride, B. J., and Zeleznik, F. J., "Computer program for calculation of complex chemical equilibrium composition and applications, supplement I-Transport Properties," *NASA TM-86885*, 1984. 35

[106] Morley, C., "Gaseq," `http://www.gaseq.co.uk`, Accessed: 2022-11-16. 35

[107] "Ansys Chemkin-Pro," `https://www.ansys.com/products/fluids/ansys-chemkin-pro`, Accessed: 2022-11-16. 36

[108] "Cantera," `https://www.cantera.org`, Accessed: 2022-11-16. 36

[109] Sun, W. and Yuan, Y.-x., *Optimization Theory and Methods*, Springer, 2006. 39, 40

[110] Bousson, K., "Métodos e Algoritmos de Otimização Paramétrica. Master's Degree Lecture Notes on Trajectory Optimization and Control," Department of Aerospace Sciences, University of Beira Interior, Covilhã, Portugal, 2020. 39, 40

[111] Vadlamani, S. K., Xiao, T. P., and Yablonovitch, E., "Physics successfully implements Lagrange multiplier optimization," *Proceedings of the National Academy of Sciences*,

Vol. 117, No. 43, oct 2020, pp. 26639–26650. 41, 42

[112] Corriou, J.-P., *Numerical Methods and Optimization*, Vol. 187 of *Springer Optimization and Its Applications*, Springer International Publishing, 2021. 42

[113] White, W. B., Johnson, S. M., and Dantzig, G. B., "Chemical Equilibrium in Complex Mixtures," *The Journal of Chemical Physics*, Vol. 28, No. 5, may 1958, pp. 751–755. 42, 43, 45

[114] Blecic, J., Harrington, J., and Bowman, M. O., "TEA: A Code for Calculating Thermochemical Equilibrium Abundances," *The Astrophysical Journal Supplement Series*, Vol. 225, No. 1, jul 2016, pp. 4. 42, 44, 45

[115] Cassel, K. W., *Matrix, Numerical, and Optimization Methods in Science and Engineering*, Cambridge University Press, jan 2021. 45, 46

[116] Beu, T. A., *Introduction to Numerical Programming A Practical Guide for Scientists and Engineers Using Python and C/C++*, Taylor & Francis Group, 2014. 46, 47

[117] Chapra, S. C. and Canale, R. P., *Numerical methods for engineers*, McGraw-Hill, 2009. 47

[118] McBride, B. J., Zehe, M. J., and Gordon, S., "NASA Glenn Coefficients for Calculating Thermodynamic Properties of Individual Species," Tech. rep., National Aeronautics and Space Administration, John H. Glenn Research Center at Lewis Field Cleveland, Ohio 44135–3191, Sept. 2002. 48

[119] Eriksson, G., Holm, J. L., Welch, B. J., Prelesnik, A., Zupancic, I., and Ehrenberg, L., "Thermodynamic Studies of High Temperature Equilibria. III. SOLGAS, a Computer Program for Calculating the Composition and Heat Condition of an Equilibrium Mixture." *Acta Chemica Scandinavica*, Vol. 25, 1971, pp. 2651–2658. 48

[120] Westbrook, C. K. and Dryer, F. L., "Chemical kinetic modeling of hydrocarbon combustion," *Progress in Energy and Combustion Science*, Vol. 10, No. 1, jan 1984, pp. 1–57. 49

[121] Yetter, R. A., Dryer, F. L., and Rabitz, H., "A Comprehensive Reaction Mechanism For Carbon Monoxide/Hydrogen/Oxygen Kinetics," *Combustion Science and Technology*, Vol. 79, No. 1-3, sep 1991, pp. 97–128. 49

[122] Law, C. K., Makino, A., and Lu, T. F., "On the off-stoichiometric peaking of adiabatic flame temperature," *Combustion and Flame*, Vol. 145, No. 4, jun 2006, pp. 808–819. 55, 57